

Towards the Secondary Bar: Gas Morphology and Dynamics in NGC 4303

Eva Schinnerer

*Department of Astronomy, MS 105-24, California Institute of Technology, Pasadena, CA
91125*

es@astro.caltech.edu

Witold Maciejewski

*Osservatorio Astrofisico di Arcetri, Largo E. Fermi 5, 50125 Firenze, Italy, and
Obserwatorium Astronomiczne Uniwersytetu Jagiellońskiego, Poland*

witold@arcetri.astro.it

Nick Scoville

*Department of Astronomy, MS 105-24, California Institute of Technology, Pasadena, CA
91125*

nzs@astro.caltech.edu

and

Leonidas A. Moustakas

*Dept. of Astrophysics, Nuclear and Astrophysics Laboratory, University of Oxford, 1 Keble
Road, Oxford OX1 3RH, UK*

leonidas@astro.ox.ac.uk

ABSTRACT

We report on the molecular gas properties in the central kiloparsec of the almost face-on double barred galaxy NGC 4303 (M 61), using the ^{12}CO 1–0 line emission observed with the Owens Valley Radio Observatory (OVRO) millimeter interferometer. The bulk of the molecular line emission comes from two straight gas lanes which run north-south along the leading sides of the large-scale primary bar. Velocity deviations of up to 90 km s^{-1} from the mean rotational velocity are associated with these gas lanes. Inside a radius of $\sim 5''$ ($\sim 400 \text{ pc}$) the molecular

gas forms a spiral pattern which, for the northern arm, can be traced to the nucleus. The high angular resolution of our OVRO data ($2'' \sim 150$ pc), together with archival HST data, allows for a comparison with dynamical models of gas flow in the inner kiloparsec of single- and double-barred galaxies. We find that the observed global properties of the molecular gas are in agreement with models for the gas flow in a strong, large-scale bar, and the two-arm spiral structure seen in ^{12}CO in the inner kiloparsec can already be explained by a density wave initiated by the potential of that bar. Only a weak correlation between the molecular gas distribution and the extinction seen in the HST $V - H$ map is found in the inner 400 pc of NGC 4303: The innermost part of one arm of the nuclear ^{12}CO spiral correlates with a weak dust filament in the color map, while the overall dust distribution follows a ring or single-arm spiral pattern well correlated with the UV continuum. This complicated nuclear geometry of the stellar and gaseous components allows for two scenarios: (A) A self-gravitating $m = 1$ mode is present forming the spiral structure seen in the UV continuum. In this case the gas kinematics would be unaffected by the small ($\sim 4''$) inner bar. (B) The UV continuum traces a complete ring which is heavily extinguished north of the nucleus. Such a ring forms in hydrodynamic models of double bars, but the models cannot account for the UV emission observed on the leading side of the inner bar. Comparison with other starburst ring galaxies where the molecular gas emission and the star forming clusters form a ring or tightly wound spiral structure suggests that the starburst ring in NGC 4303 is in an early stage of formation.

Subject headings: galaxies: nuclei – galaxies: ISM – galaxies: kinematics and dynamics – galaxies: individual(NGC 4303)

1. INTRODUCTION

Recent studies show that about 75% of all spiral galaxies have bars, and out of those, some 40% have at least one inner (second) bar (see e.g. Laine et al. 2002, Erwin & Sparke 2002). The inner bar appears randomly oriented with respect to the outer, main, bar (e.g. Buta & Crocker 1993), indicating that the two bars may rotate independently. Such systems of nested bars may funnel galactic gas towards an active galactic nucleus (AGN), as proposed by Shlosman, Frank & Begelman (1989). However, Shlosman et al. considered only gaseous inner bars resulting from the instability in the nuclear disk. Detection of nuclear bars in the near infrared (e.g. Jungwiert, Combes & Axon 1997) indicates that their predominant

component may be stellar. Friedli & Martinet (1993) investigated the stability of stellar double bars, and found that such systems can survive for a few rotations after the two bars decouple. Recently, Rautiainen & Salo (1999) showed that various modes, such as spiral arms and multiple bars, can coexist for several Giga-years. Maciejewski & Sparke (2000) found orbital families that can support double bars, and that are related to the x_1 and x_2 orbits in single barred galaxies. They predicted that gas flows in dynamically possible stellar nested bars lack straight shocks in the inner bar, and do not involve strong gas inflow; they therefore differ significantly from the instability scenario proposed by Shlosman et al. Given this discrepancy, it is important to observe the molecular gas in double barred galaxies, so that its morphology and kinematics can be confronted with the diverging dynamical scenarios.

Detailed comparison of individual galaxies with high-resolution dynamical models allows us to explore the mechanisms of gas transport on large and small scales. Gas condensations in lanes running along the leading side of a large-scale bar in the models of Athanassoula (1992) are observed as dust lanes in a number of galaxies. Recent dynamical models by Englmaier & Shlosman (2000) for the gas flow in the inner kiloparsec of a barred galaxy showed that an induced gas density wave could form a grand-design structure. A recent HST survey of the nuclear regions of nearby Seyfert galaxies shows that spiral structures (either grand-design or flocculent) are common in the central kiloparsec (Pogge & Martini 2002).

Despite the progress in modeling, few observations of the gas flow in double barred galaxies exist to-date which allow one to carefully test the validity of the theoretical assumptions. An almost face-on inclination is favored for comparisons to dynamical models, since deprojection effects are minimized. Furthermore, the bars should not lie close to the kinematic major or minor axes in order that non-circular motion can be more easily studied. For our study, we selected the nearly face-on galaxy NGC 4303 (M 61).

NGC 4303 is probably associated with the Virgo cluster (Binggeli, Sandage & Tammann 1985). A large-scale bar of about $40''$ (Laine et al. 2002) lies inside the outer spiral arms. In addition to the large-scale bar, NGC 4303 hosts a second, inner bar of about $4''$ length which is surrounded by a circumnuclear starburst ring/spiral of $6''$ (~ 0.5 kpc) diameter (Colina & Wada 2000, Perez-Ramirez et al. 2000, Colina et al. 1997). A high-angular resolution HST UV image shows several compact star forming regions within this ring. The starburst ring dominates the integrated UV output of NGC 4303 (Colina et al. 1997). The nucleus is classified as a LINER/Seyfert 2 type (Ho, Filippenko & Sargent 1997). For consistency with the work by Colina et al. (1997, 1999, 2000), we adopt the distance of M 100, the brightest spiral in the Virgo cluster (16.1 Mpc, Ferrarese et al. 1996; $1'' \approx 78$ pc).

The paper is organized as follows: After a brief description of the observations in Section 2, the kinematic and dynamical quantities directly derivable from our mm-interferometric data are presented in Section 3. In Section 4, the molecular gas distribution is compared to the stellar properties in the inner kiloparsec, and the bar properties as well as the dynamical resonances are derived. In Sections 5 and 6 we interpret the observed gas morphology and kinematics in the framework of available dynamical models. Implications and discussion are presented in Section 7, followed by the Summary and Conclusions in Section 8.

2. OBSERVATIONS

2.1. Millimeter Interferometric Observations

NGC 4303 was observed in its ^{12}CO 1 – 0 line between 1999 December and 2000 March using the Owens Valley Radio Observatory (OVRO) millimeter interferometer with six 10.4 m telescopes in its E, H and U configurations. The resulting baselines range from 30 m to 480 m providing a spatial resolution of $\sim 2.0''$ (150 pc) with natural weighting (beam size: $2.22'' \times 1.84''$ with PA of 84.3°). Two spectrometer modules were utilized resulting in 120 channels with a spectral resolution of 5.2 km s^{-1} per channel. The quasar 3C273 served as a passband and phase calibrator and was observed every 20 minutes. The average single sideband temperature was around 800 K at the observed line frequency of 114.67 GHz. The resulting noise per channel is $\sim 25 \text{ mJy beam}^{-1}$ in the combined data of the 3 tracks. (The two channels at velocities of 1596 km s^{-1} and 1574 km s^{-1} have a slightly higher r.m.s. due to the reduced sensitivity at the edge of one spectrometer module.) The data were calibrated using the OVRO software package MMA (Scoville et al. 1993). The final ^{12}CO cube was mapped and deconvolved using the CLEAN algorithm within the software package MIRIAD (Sault et al. 1995). For the deconvolution we used defined CLEAN regions, 10000 iterations, a gain of 0.0075 and a 1σ cutoff level of 25 mJy beam^{-1} , thus allowing for a proper reduction of the beam effects in the dirty cube. Side lobe artifacts might dilute the line emission seen in the straight gas lanes running in north-south direction, as the dirty beam has side lobes at the 35% level about $6''$ north and south of the center due to the low declination of the source ($\sim 4^\circ$; Fig. 2). However, since we detected no line emission above the 5σ level in the channel maps (Fig. 5) on the opposite sites of the gas lanes, we are confident that all prominent side lobes artifacts have been removed. Further analysis (moment maps, flux measurements, rotation curve fitting) was performed using the radio software package GIPSY (van der Hulst et al. 1992). The data cubes were corrected for the response of the primary beam, since the outer emission peaks coincide with the half power beam width (HPBW) of the OVRO dishes. The (biased) moment maps were made using a clipping level of 3σ with the restriction that

emission above the clipping level is at least present in two adjacent channels in the primary beam corrected data cube.

2.2. HST Archival Data

Through the STScI HST Archive we obtained high resolution imaging data of the nuclear region of NGC 4303. The datasets are summarized in Table 1, and include HST/WFPC2 data in the F606W filter, HST/NICMOS (Camera 2) imaging in the F160W filter (see also Colina & Wada 2000), and HST/STIS imaging with the STIS/NUV-MAMA detector (P.I. Colina). We used standard reduction procedures. The optical image was resampled to the pixel scale of NIR image. All images were registered to match the location of the bright central source with the H band peak emission. The registration of all images was checked on the dusty regions and the stellar clusters, and showed good agreement ($\ll 1''$).

3. THE INTERFEROMETRIC DATA ON THE MOLECULAR GAS

3.1. Distribution

The molecular gas emission is concentrated in two straight gas lanes running north and south of the nucleus (Fig. 1 and 2). These gas lanes show a lateral offset from the nucleus of about $7''$ and curl towards the nucleus inside a radius of $r \sim 5''$. The distribution of the molecular gas emission is not smooth, showing local contrasts of more than a factor of four within the gas lanes. In addition, two peaks of emission about $28''$ (2.0 kpc) north and south of the nucleus are present (see Fig. 3). Comparison of spectra extracted for these peaks with the nuclear region rule out the possibility that these peaks could arise from side lobe artifacts due to the low declination of the source (Fig. 4). Those peaks clearly show a velocity shift of the line centers. The geometry of the molecular gas as observed in the ^{12}CO 1 – 0 line emission is reminiscent of the dust lane structures seen in simulations of the gas response in a barred potential (e.g. Fig. 2 of Athanassoula 1992; hereafter A92; see Section 5).

3.2. The kinematics

The ^{12}CO 1 – 0 velocity field in the inner $12''$ appears regular in most locations, consistent with the “spider” diagram expected for a differently rotating disk (Fig. 2 and Fig. 5). The line of nodes changes at a radius of $\sim 7''$ between the inner region and the gas

lanes indicating the presence of non-circular motions. This can also be seen in the channel maps (Fig. 5) where the molecular gas in the lanes moves almost in north-south direction whereas in the inner $8''$ the gas emission moves from south-east to the north-west. The distribution of the velocity dispersion in the 2nd moment map is relatively smooth with an average value of $\sim 10 \text{ km s}^{-1}$ throughout the observed region (Fig. 2).

The position-velocity (pv) diagram along the kinematic major axis shows a steep rise in velocity to a distance of $r \sim 4''$. There is good agreement with the $\text{H}\alpha$ pv diagram for the same position angle (Rubin et al. 1999; also Fig. 7). The deviations are probably due to the slightly different angular resolution and the higher spectral resolution of the ^{12}CO data. Comparison with stellar absorption line data along a position angle of $\text{PA} = 342^\circ$ (Heraudeau et al. 1998) shows that the velocity of the stars is much lower. It is unlikely that this is due to non-circular gas motions in the inner $\sim 10''$, as the ^{12}CO velocity field (Fig. 2) as well as the $\text{H}\beta$ velocity field (Colina & Arribas 1999) are similar to a smoothly rotating disk with radial motions of less than 10 km s^{-1} (Colina & Arribas 1999). The lower velocity of the stars in the central region very likely reflects the fact that the stars have a different 3-dimensional distribution, and therefore different kinematics. This is consistent with large velocity dispersions of the stellar absorption lines ($\sim 80 \text{ km s}^{-1}$; Heraudeau et al. 1998) compared to those of ^{12}CO gas emission lines ($20 - 30 \text{ km s}^{-1}$; Fig. 6) in the nuclear region. A similar behavior is seen in NGC 1068 where the derived stellar rotation curve has lower velocities than the rotation curve derived from the ^{12}CO data and the $\text{H}\alpha$ line emission (Schinnerer et al. 2000a).

3.3. Dynamical reference parameters

Before a rotation curve can be fit to the ^{12}CO data, the major axis position angle and inclination, the dynamical center, and the systemic velocity need to be determined. We used an iterative approach to obtain these parameters by fitting tilted annuli to the observed ^{12}CO velocity field. For the fit we weighted points closer to the major kinematic axis higher and neglected regions that lie within 15° of the minor axis. We used the routine ‘ROTCUR’ in GIPSY, in which only the rotation velocity and one parameter were fit at a time, keeping all other parameters fixed.

Position angle and inclination: We estimate a position angle of $(317 \pm 5)^\circ$ for the inner $10''$, where the ^{12}CO velocity field should not be disturbed by the bar potential. This agrees with Guhathakurta et al. (1988), who obtained a position angle of $(318 \pm 5)^\circ$ from a fit to the large scale HI velocity field, and with Colina & Arribas (1999), who find a position angle of $\sim (310 \pm 4)^\circ$ from modeling the $\text{H}\beta$ velocity field in the inner $8''$. A

robust determination of the inclination is difficult because of the almost face-on aspect of NGC 4303 and the optical disk disturbed due to tidal interaction with two nearby companions (NGC 4292 and NGC 4303A; Binggeli et al. 1985). From the optical images of Frei et al. (1996) using the lowest undisturbed contours (excluding the regions of the spiral arms), we derive an inclination of $\sim 25^\circ$ by excluding radii that are already affected by the bar which has a position angle of $\sim 10^\circ$. A fit to the ^{12}CO velocity field in the inner $20''$ gives an inclination of $i = (21 \pm 10)^\circ$. Cayatte et al. (1993) find a similar value, and Ma, Peng & Gu (1998) obtain 22° from a fit to the spiral structure. Note that Colina & Arribas (1999) used an inclination of $\sim 45^\circ$ assuming that the ionized gas structure of the inner $8''$ is circular. However, as it seems unlikely that the inner $8''$ disk has a different inclination, we adopt the value for the outer disk of 25° , which is consistent with the inclination derived from the ^{12}CO velocity field, and we use a position angle of 318° to fit the rotation curve.

The dynamical center: Direct measurements of the dynamical center from the ^{12}CO line data is complicated by the fact that the line emission is not smoothly distributed in the inner $8''$. Nevertheless, since the gas distribution appears point-symmetric, the bar potential producing this pattern is plausibly expected to be point-symmetric as well with respect to the dynamical center. If we assume that the two gas lanes are symmetrically distributed about the nucleus, we find that the dynamical center of the galaxy is located within $1''$ of the central peak in the NICMOS F160W image. (We verified this by aligning the dust lanes seen in the HST F606W image and the gas lanes.) Thus the dynamical center is identical with the peak of the old stellar population as seen in the F160W image. We therefore adopt $12:21:54.99 +04:28:25.6$ (J2000.0) as the dynamical center for fitting of the rotation curve.

Systemic velocity: We find a systemic velocity of $v_{\text{LSR}} = (1559 \pm 3) \text{ km s}^{-1}$ using tilted ring fitting. This translates into $v_{\text{helio}} = v_{\text{LSR}} + 9.5 \text{ km s}^{-1} = 1569 \text{ km s}^{-1}$ for NGC 4303. Previous measurements in the HI line gave $v_{\text{helio}} = (1568 \pm 6) \text{ km s}^{-1}$ with the WSRT (Westerbork Synthesis Radio Telescope) at an angular resolution of $10''$ (Warmels 1988), and $(1566 \pm 5) \text{ km s}^{-1}$ with the VLA (Very Large Array) at an angular resolution of $45''$ (Guhathakurta et al. 1988). Our value is in very good agreement with the HI systemic velocity. The lower value of $v_{\text{helio}} = 1552 \text{ km s}^{-1}$ from the modeling of the $\text{H}\beta$ velocity field (Colina & Arribas 1999) might be due to the lower spectral resolution of the $\text{H}\beta$ data. We used a value of $v_{\text{LSR}} = 1560 \text{ km s}^{-1}$ to fit the rotation curve.

3.4. Rotation curve and dynamical mass

Since the molecular line emission in NGC 4303 is distributed very unevenly throughout the disk, it is very difficult to obtain an optimally averaged rotation curve. In addition,

from the gas morphology we expect strong non-circular motions in the straight gas lanes. Therefore the rotation curve that we derive here is strongly biased towards regions with higher emission, and is more representative of the streaming motion outside the inner $10''$. On the other hand, the coverage of the inner $10''$ is complete enough to give a good estimate of the averaged rotation curve representing the underlying gravitational potential.

Two methods were used to obtain the rotation curve (Fig. 8): A least square fit to the velocity field using inclined rings (routine ‘ROTCUR’) and a direct fit to pv diagrams along eight different position angles separated by steps of 22.5° for a good coverage of the galaxy disk (routine ‘INSPECTOR’). The latter method allowed us to examine the effect of beam smearing. In this procedure, a rotation curve is obtained by fitting a tilted ring model to the whole data cube by comparing the model with the pv diagrams. This method is more robust against multiple line components or additional non-circular components. It also allows us to fit the rotation curve to the two outer ^{12}CO emission peaks at a radius of $r \sim 28''$. As discussed above, the dynamical center, the systemic velocity ($v_{\text{sys}} = 1560 \text{ km s}^{-1}$), the position angle ($\text{PA} = 318^\circ$) and the inclination ($i = 25^\circ$) were kept fixed.

In the case of NGC 4303 the two rotation curves agree very well with each other for the inner $r \leq 15''$ (Fig. 8). The only discrepancy is the peak velocity at a radius of $r \sim 4''$ which is about 20 km s^{-1} higher for the rotation curve derived by ‘INSPECTOR.’ This is expected, since this method is less affected by beam smearing. The derived velocity value at $r \sim 4''$ from the $\text{H}\beta$ velocity field (Colina & Arribas 1999) is in very good agreement with the ^{12}CO rotation curve when corrected for the different assumed inclinations of the disk (see Section 3.3). The drop of the rotation velocity from $v(r = 4'') \sim 150 \text{ km s}^{-1}$ to $v(r = 18'') \sim 75 \text{ km s}^{-1}$ is sub-Keplerian (Fig. 8). Thus, the derived rotation velocity can only be regarded as a lower limit. This behavior confirms the presence of strong non-circular motion for radii between $r \sim 4'' - 30''$. Therefore, we assume a constant rotation velocity of 150 km s^{-1} between $r = 4'' - 30''$. For larger radii the ^{12}CO , $\text{H}\alpha$ (Rubin et al. 1999) and HI (Cayatte et al. 1990) rotation velocities are consistent.

We constructed a model velocity field from the derived rotation curve. The residual velocity field of the observed minus the model field (Fig. 9) shows differences of $\sim 7 \text{ km s}^{-1}$ at the outer ^{12}CO peaks, and $\sim 5 - 10 \text{ km s}^{-1}$ in the inner $12''$ where the ^{12}CO emission starts to form a spiral-like structure. Therefore, the ^{12}CO line emission is well approximated by a rotating disk with the derived rotation curve in the inner $12''$. Outside that region, along the gas lanes, a maximum value for the residual velocities of about $25 - 30 \text{ km s}^{-1}$ is found at a radius of $\sim 9.5''$ ($\approx 740 \text{ pc}$) which is about the position of the inner Lindblad resonance (ILR; see Section 5). After correcting for inclination, these values translate into $\sim 60 \text{ km s}^{-1}$ which is the difference between the ^{12}CO rotation velocity and the adopted rotation curve.

If the spiral arms are trailing, NGC 4303 is rotating clockwise and the north-eastern side is the near side of the galaxy disk. As negative residuals are found in the north-western gas lane and positive residuals in the south-eastern gas lane this is consistent with strong inflowing motions, as predicted by numerical simulations of gas flow in a barred potential (e.g. A92; Piner et al. 1995; for a detailed explanation see also Regan, Sheth & Vogel 1999). This situation is similar to the findings of Regan et al. (1999) for NGC 1530.

The dynamical mass $M(r)$ can be derived for the inner $8''$ where the measured rotation curve agrees with solid body rotation using $v^2(r) = G \frac{M(r)}{r}$ where $v(r)$ is the measured circular velocity (G is the Gravitational constant). For $v(r = 4'') \approx 150 \text{ km s}^{-1}$ we get a dynamical mass $M_{\text{dyn}}(r = 4'') \approx 1.6 \times 10^9 M_{\odot}$.

3.5. Molecular Gas Masses

The $^{12}\text{CO } 1 - 0$ line fluxes S_{CO} for several regions (nucleus, inner disk, inner spiral arms, inner and outer gas lanes, and the outer peaks as indicated in Fig. 3) are summarized in Table 3. The total line flux of $\sim 210 \text{ Jy km s}^{-1}$ detected by the interferometer can be compared to the single dish flux of $\int T_{\text{A}}^* dv = (11.9 \pm 2.1) \text{ K km s}^{-1}$ detected at the center with the FCRAO 14m (Kenney & Young 1988). Without any assumptions and corrections for the size of the molecular gas disk, this translates into $\sim 520 \text{ Jy km s}^{-1}$. Therefore the interferometer detects only about 40% of the single dish flux. Kenney & Young (1988) give a total $^{12}\text{CO } 1 - 0$ line flux of $(2280 \pm 470) \text{ Jy km s}^{-1}$ for the whole galaxy using several single dish pointings, so that the molecular gas emission mapped by the interferometer comprises only about 10% of the total molecular gas present. A recent BIMA SONG (Survey of Nearby Galaxies) map of NGC 4303 with several pointings shows a large fraction of the molecular gas along the outer spiral arms (Sheth 2001). This indicates that a large-scale disk of molecular gas is present, and that the molecular gas in the spiral disk of NGC 4303 is only partially redistributed towards the nucleus.

We used the $\frac{N_{\text{H}_2}}{I_{\text{CO}}}$ conversion factor of $2 \times 10^{20} \text{ cm}^{-2} (\text{K km s}^{-1})^{-1}$ from Strong et al. (1987) to derive molecular gas masses. Note, that the value of the $\frac{N_{\text{H}_2}}{I_{\text{CO}}}$ conversion factor has an uncertainty of a factor of 2 - 3 (see e.g. Meier, Turner & Hurt 2000; Weiß et al. 2001). The molecular gas in the inner $8''$ ($\sim 630 \text{ pc}$) has a mass of about $M_{\text{H}_2} \sim 7 \times 10^7 M_{\odot}$ (excluding the uncertainty of the conversion factor), which is about $\sim 4\%$ of the dynamical mass of $\sim 1.6 \times 10^9 M_{\odot}$. Close to the nucleus about $10^7 M_{\odot}$ of molecular gas are present. The amount of molecular gas mass in the two prominent parts of the straight gas lanes is about twice the amount in the inner 630 pc .

3.6. Molecular gas disk scale height

There are various ways to estimate the velocity dispersion in the inner $8''$ of the molecular gas disk. The velocity dispersion is about $10 - 15 \text{ km s}^{-1}$ in the 2nd moment map which can be regarded a lower limit due to the 3σ clipping which was used to derive the map. The spectra in the nuclear region (Fig. 6) show average line widths of $15 - 30 \text{ km s}^{-1}$ which are a better measure of the observed velocity dispersion. If the inner molecular gas ‘disk’ is in hydrostatic equilibrium, the velocity dispersion of the molecular gas, after correcting for the rotational contribution due to the finite beam size, can be used to derive a disk scale height. The observable velocity gradient is $\sim 15 \text{ km s}^{-1} \text{ arcsec}^{-1}$ in the inner $8''$ (using the observed velocity of $v(r = 4'') \sim 63 \text{ km s}^{-1}$). The true velocity dispersion is then $15 - 20 \text{ km s}^{-1}$ using quadratic deconvolution to correct for the contribution from the rotation velocity. Several theoretical relations between the velocity dispersion and the disk height can be found in the literature. Quillen et al. (1992; their equation 3.1) and Combes & Becquaert (1997; third equation in their introduction) have derived such relations for gas disks in potentials similar to the ones of elliptical galaxies or galaxy bulges. With the true velocity dispersion of $15 - 20 \text{ km s}^{-1}$, and a rotational velocity $v(4.0'') \approx 150 \text{ km s}^{-1}$ as well as the associated molecular and dynamical masses, we find a disk thickness of about $25 - 30 \text{ pc}$ at a radius of $r \sim 4'' \approx 300 \text{ pc}$. This is similar to the low molecular gas disk scale heights found in the central few 10 pc in the two nearby Seyfert galaxies NGC 1068 and NGC 3227 (Schinnerer et al. 2000a,b).

4. THE OBSERVED STELLAR AND DYNAMICAL PROPERTIES OF NGC 4303

4.1. Dust extinction and star formation in the inner kiloparsec

In the inner kiloparsec, two or three dust lanes running from east to north are present in the $V - H$ color map (Fig. 10). The eastern end of the outermost dust lane coincides with the northern gas spiral arm seen in ^{12}CO at our resolution of $2''$. Directly north of the nucleus, the dust lane splits into two: a fainter part follows the ^{12}CO pattern, but its much clearer extension continues into the ring-like blue feature. This feature appears also in the UV continuum as a string of young stellar clusters forming the starburst ring or spiral at $r \sim 2.5''$ (200 pc) (Fig. 10; see also Fig. 1 of Colina et al. 1997). This continuation suggests that the ring might be more extinguished towards the northern part, or that the star formation is weaker in the north of the ring, and ceases at the dust lane (see also section 6). In a second scenario, the northern molecular spiral continues inwards, and is seen as a dust

lane, with star formation starting at still smaller radii. It is interesting to note that if the UV morphology is interpreted as a spiral, it is a *single-arm* spiral originating from the northern molecular spiral arm. The young stellar clusters are offset from the molecular gas distribution next to the disturbed, southern molecular spiral arm. This arm discontinues in ^{12}CO at $\text{PA} \sim 135^\circ$, and finds no continuation in other features, aside possibly for the second eastern dust lane, which appears almost straight in the V-H color map. It appears that Apparently, the massive star formation next to the southern molecular arm has affected the gas distribution in that region (see Section 7.2).

Colina & Wada (2000) derive an excess extinction of about 1.7^{mag} for the northern dust lane relative to values for face-on spiral galaxies, similar to values observed in the circumnuclear regions of other spiral galaxies (e.g. Regan & Mulchaey 1999; Martini & Pogge 1999). This translates into an extinction of about 20^{mag} in the UV band using the effective extinction law derived for the stellar continuum in starburst galaxies (Calzetti, Kinney & Storchi-Bergmann 1994). This high extinction in the northern dust lane would be enough to obscure any UV cluster in this region, thus it seems possible that the star formation might actually occur in the ring traced by the UV clusters and the prominent (northern) dust lane.

Comparison with the optical line, and the optical and NIR continuum emission suggests that the stellar clusters are between 5 – 25 Myr old and have stellar masses of about $(0.5 - 1.0) \times 10^5 M_\odot$ (Colina & Wada 2000). Colina & Wada (2000) noted that the UV knots east of the inner bar are older ($\sim 10 - 25$ Myr) and more massive (up to $2.3 \times 10^5 M_\odot$) than the ones west of the NIR bar ($\sim 2.5 - 7.5$ Myr), suggesting an age trend within the star forming ring. The molecular spiral arms can be divided into about six individual clumps with molecular gas masses of $M_{H_2} \sim 7 \times 10^6 M_\odot$ and sizes between $\leq 2''$ and $3''$ ($\leq 150 - 230$ pc), typical for GMC complexes (the 0th moment map is sensitive to cloud masses above $10^6 M_\odot$). The star formation efficiency (SFE) for a molecular cloud lies typically between 3% (for the total cloud including low-mass star formation) and 24% (for the hot cores; see review by Elmegreen et al. 1999). If one allows for an elevated SFE of about 10% in the circumnuclear region, which seems plausible given the different physical properties compared to the disk of galaxies, then a single massive GMC complex similar to those observed in NGC 4303 could be a sufficient to form a dozen stellar clusters with an average stellar mass of $0.7 \times 10^5 M_\odot$ (Colina & Wada 2000) as inferred from the UV continuum (see section 7.2).

Colina & Arribas (1999) isolated a second velocity component in the [O III] line which has a velocity field almost perpendicular to that of the molecular gas. They interpret this as the signature of an ionization cone which is observed in a number of AGNs (e.g. Schmitt & Kinney 1996). Since the north-east side is the near side of the galaxy, the ionization

cone is in front of the south-western part of the galaxy disk. The obvious asymmetry in the extinction in the inner $8''$ could be then partly due to the presence of an ionization cone most affecting the region south-west of the nucleus. This suggests that the circumnuclear colors in NGC 4303 are (a) strongly modified by the varying colors of the different stellar populations (the clusters are obvious in the $V - H$ map), and that (b) an ionization cone might affect the overall distribution of the extinguishing material. This cautions the interpretation of dust features seen in HST color maps as being only due to molecular gas condensations.

4.2. The bar properties

The large-scale bar in NGC 4303 runs almost north-south ($PA \sim 10^\circ$) inside the spiral arms. Martin (1995) and Chapelon et al. (1999) find its semi-major axis length to be about $a \approx 20''$. Laine et al. (2002) revised this result and obtained a deprojected semi-major axis length of $a \approx 47''$ (≈ 3.5 kpc) and a deprojected axial ratio of $b/a \sim 0.34$. Because of the large discrepancy between these results, we fit ellipses to the *gri* images of Frei et al. (1996) and find a semi-major axis length between $30''$ and $40''$. A more exact determination of the scale length is hampered by the resolution of the Frei et al. data and the fact that the spiral arms start at a radius of $\sim 40''$, which must be close to the end of the bar. Since our value for the semi-major axis appears to be more consistent with the dynamical models where the peak gas density is close to the end of the bar (see Section 5), we assume a deprojected semi-major axis length of $30'' \leq a \leq 40''$. With its axial ratio the bar is considered a strong bar, as defined by Friedli & Martinet (1993). The large-scale spiral arms are sites of massive star formation as can be seen in the $H\alpha$ line emission (Banfi et al. 1993, Koopmann, Kenney & Young 2001). However, no prominent $H\alpha$ line emission is found along the bar. This is in agreement with model predictions that the shear along *strong* bars can be too high for stars to form.

The secondary bar with a deprojected semi-major axis length of $\sim 2.2''$ (170 pc) is visible in the HST H band image inside the stellar clusters (Colina & Wada 2000; also Fig. 10). The deprojected axial ratio of the inner bar of $b/a \sim 0.73$ (Perez-Ramirez et al. 2000) is at the high end of observed ratios for secondary bars (Jungwiert, Combes & Axon 1997). If the observed axial ratio is not diluted by the underlying bulge component it indicates a weaker bar potential for the secondary bar relative to the primary bar. A string of faint star-forming clusters can be seen in the UV image north of the nucleus (e.g. Fig. 10; Colina & Arribas 1999). It coincides with the leading side of the secondary NIR bar assuming it has the same rotation direction as the outer/primary bar.

The ratio between the semi-major axes of the two bars is about 15, which is at the upper

end of the observed range (Jungwiert, Combes & Axon 1997; Maciejewski & Sparke 2000; Laine et al. 2002). The deprojected position angle of the secondary bar seen in the HST *H* band image relative to the kinematic major axis is $\text{PA} \approx 80^\circ$. Therefore the two stellar bars are oriented at about $\approx 30^\circ$ with respect to each other in the plane of the host galaxy.

4.3. Position of dynamical resonances in NGC 4303

Assuming the standard relation of $r_{CR} \approx 1.2a$ (e.g. A92) between the bar semi-major axis length $a \approx 30'' - 40''$ and corotation radius r_{CR} where the angular velocity Ω is equal to the bar pattern speed Ω_P , we find that the corotation radius lies between $36''$ and $48''$. Thus the primary bar rotates with a pattern speed of about $\Omega_P \sim 40 - 53 \text{ km s}^{-1} \text{ kpc}^{-1}$.

For this pattern speed, and the rotation curve derived in Section 3.4 (see Fig 8), the large-scale bar has two ILRs. The inner ILR (iILR), when localized directly from the data, lies at $\sim 2.0''$ radius, and coincides with the semi-major axis radius of the nuclear bar ($2.2''$; Perez-Ramirez et al. 2000). This puts the corotation resonance of the inner bar between the two ILRs of the outer bar, roughly in agreement with theoretical expectations (e.g. Friedli & Martinet 1993, Maciejewski & Sparke 1997). However, the dynamically preferred scenario (Maciejewski & Sparke 2000) requires that the inner bar ends far outside the iILR of the main bar, so there is a sufficient set of orbits that can support it. We discuss this discrepancy with the observed near-overlapping of one bar’s end with the others iILR in Section 6.

The position of the outer ILR (oILR) can be determined using the adopted flat rotation curve for this radial distance as an upper measured limit (see Section 3.3). We derive the oILR to be at $10'' - 14''$ radius.

5. MOLECULAR DATA AND THE DYNAMICAL MODELS

5.1. Outer Regions: The Overall Geometry

The gas response strongly depends on the gravitational potential, and especially on the properties of the stellar bar component (A92). A large variety of possible gas morphologies is explored by A92. The overall distribution of the ^{12}CO line emission in the inner arcminute of NGC 4303 is very reminiscent of the standard model 001 by A92. The molecular gas is concentrated towards the nucleus in two narrow straight gas lanes, and in additional emission peaks close to each end of the bar. Near the nucleus the straight lanes start to curl inward resembling a structure similar to a ‘nuclear spiral’ or ‘nuclear ring’. As pointed out by A92

such behavior can only be observed if an inner Lindblad resonance (ILR) is present. The observed structure can be explained by the gas moving gradually from x_1 orbits (the family of stable periodic orbits elongated along the bar major axis) to x_2 orbits (the family of stable periodic orbits elongated along the minor bar axis; in the notation of Contopoulos 1981), which only exist in the presence of an ILR.

The amazing similarity between the A92 standard model and the ^{12}CO distribution in NGC 4303 suggests a bar strength consistent with the model axial ratio of about 0.4. This roughly agrees with the deprojected ratio of $b/a \sim 0.34$ of Laine et al. (2002). Note though that the observed value is integrated over the total light that includes the bulge, while the models give the axial ratio of the bar only. Thus the observations suggest that the axial ratio of the bar may be considerably lower than 0.4. Also, the observed angle between the straight part of the gas lanes and the bar major axis is $\sim 10^\circ$ in NGC 4303 which is half the value found for model 001 (A92). This reinforces the supposition that the actual ratio of the bar might be even lower than 0.4.

If the northern and southern emission peaks at a distance of $\sim \pm 28''$ are due to the dynamics imposed by the large-scale bar, they should lie inside the bar potential, roughly at the position of the 4:1 resonance (Englmaier & Gerhard 1997; see also Fig. 2(d) of A92). For a flat rotation curve, the 4:1 resonance occurs at 0.65 of the corotation radius, which places the corotation at $43''$ in this interpretation. This is consistent with the value that we assumed, and after dividing by 1.2 it gives the bar's semi-major axis of $36''$.

The qualitative comparison between the A92 standard model 001 and the distribution of the ^{12}CO emission in NGC 4303 shows very good agreement. The fact that some $\text{H}\alpha$ emission is associated with the two outermost emission peaks (e.g Fig. 3.3 in Sheth 2001, Fig. 5 in Koopmann, Kenney & Young 2001) is also in agreement with the model that has a factor of 6 – 10 lower shear in these regions. This is sufficiently low to allow star formation to occur (A92). The higher-resolution models of Maciejewski et al. (2002) clearly show that the gas density peaks correspond to an almost shear-free region along the bar at about the position of the 4:1 resonance. The resolution of the A92 models is, unfortunately, too coarse to allow for a direct comparison of the dynamics in the (circum)nuclear region itself.

5.2. ^{12}CO in the inner Kiloparsec

To date, only a few high-resolution dynamical calculations have been done to investigate the gas flow in the inner kiloparsec of barred galaxies. Englmaier & Shlosman (2000) studied gas response in nuclear regions of a barred potential similar to that in the standard model of

A92. They found that the velocity dispersion in the gas (which is assumed to be isothermal) together with the potential shape determines whether the gas settles on a nuclear ring, disk or spiral. In particular, high-velocity-dispersion gas forms a nuclear grand design spiral inside the ILR. This structure can be explained in terms of gas-density-wave theory as a response of non-selfgravitating gas to the torque of the bar. A gas density wave can exist inside the ILR, in a region where the torque is not too strong (the x_2 orbits are almost circular), and where no shocks are present. The pitch angle of the nuclear spiral has a strong dependence on the gas velocity dispersion, and is higher for higher sound speed, which is the measure of velocity dispersion. Maciejewski et al. (2002) noticed that although weak waves inside the ILR can be described by linear-wave theory, sometimes the strong straight shock in the large-scale bar can propagate all the way towards the center as a spiral shock, rendering the linear wave approximation invalid. Strong streaming motions seen along the gas spirals in NGC 5248 (Jogee et al. 2002) may be indicative of such a spiral shock there.

Since the nuclear molecular gas emission in NGC 4303 shows a spiral-like pattern in the inner $8''$, a detailed comparison between the ^{12}CO data and the predictions of the dynamical models by Englmaier & Shlosman (2000) was performed in order to assess how far inwards the outer bar dominates the gas dynamics. The agreement between model predictions and the data is surprisingly good given the fact that no tailored models with the exact galaxy parameters are used.

Rotation curve: The azimuthal velocity of the molecular gas decreases in the region where the shock is strongest, i.e. close to the ILR, creating a net inflow. It is very reminiscent of Fig. 8 of Englmaier & Shlosman (2000). Although that figure displays velocities at the maximal gas condensation, our derived ^{12}CO rotation curve of NGC 4303 is also strongly biased towards bright emission, and thus can be explained by inflow in a strong bar in the context of the models. Comparing our curve to the model one, we find that inside a radius of $r \sim 4''$ where the rotation curve is rising, the ^{12}CO rotation curve can be used as a tracer for the dynamical mass. According to the model, the (outer) ILR coincides with the largest difference between the rotation curve and the azimuthal velocity. Since there are no other measurements of the rotation velocity in NGC 4303 with sufficient angular resolution, the oILR can be placed at a radius between $10''$ and $15''$ where our measured ^{12}CO rotation velocity is lowest. This location agrees well with the estimate in Section 4.2, for which we assumed a constant rotation speed.

Density distribution: The models predict that the arm-interarm contrast in the nuclear spiral is much smaller than the contrast between the straight shock and the surrounding disk (see Fig. 4 of Englmaier & Shlosman 2000). A similar behavior is observed in NGC 4303 (Fig. 12). The arm-interarm density contrast *inside* the transition radius $R_t \approx 5''$ is about

two in NGC 4303, as is found for the model¹. However, the contrast between the straight outer shock and the outer disk in NGC 4303 is about three times higher than in the model. As noted by Englmaier & Shlosman (2000) their plot shows only a lower limit as the outer shocks are unresolved in their model. The gas lanes in NGC 4303 are unresolved in our ¹²CO data, implying that they must be significantly narrower than 150 pc (2"). The dust feature in the HST *V* band image suggests a width of about 1.5" (120 pc). This implies that the contrast should be even higher. On the other hand, for deriving the arm-interarm contrast we assumed that there is no low-level smooth large-scale emission present between the gas lanes. Since we detect only about 40% of the single dish flux, this assumption is not completely correct. For example, the effect of such a smooth component at the 1 σ level would be to lower the contrast by about a factor of three for larger radii. Therefore, the measured arm-interarm contrast is very likely a good approximation. A factor of 1.5 higher velocity dispersion is found for the density peaks within the gas lanes compared to the average dispersion of 10 km s⁻¹ in the rest of the gas lanes (Fig. 2), which might be due to the high shear in these regions. This may imply that the velocity dispersion is higher in the denser regions past the shock, and may put constraints on the post-shock star formation, e.g. may limit cluster sizes. In contrast to other barred galaxies almost no H α emission is seen along the bar (e.g. Sheth 2001), despite the high molecular gas density.

Pitch angle: The behavior of the pitch angle in a spiral arm can be a clear diagnostic for the presence of a gas density wave (Englmaier & Shlosman 2000). In our case, the gas pitch angle drops for radii between the ILR and the transition radius R_t , presumably due to the transition from x_1 to x_2 orbits (Fig. 13). Inside the transition radius the pitch angle rises again, indicating that another mechanism — a gas density wave — is responsible for the spiral structure. Measuring the pitch angle is complicated by the fact that the spiral structure in the ¹²CO line emission is not continuous. In addition the southern nuclear spiral shows distortions which are probably related to the ongoing star formation in the UV ring (see Section 4). In order to measure the pitch angle, the 0th moment map was deconvolved using the LUCY algorithm with 1000 iterations and deprojected afterwards. The pitch angle was measured by eye fitting a tangent to the spiral structure at several radii. To verify the result, the spiral structure seen in the ¹²CO emission is locally fitted by various logarithmic spirals with a constant pitch angle (40°, 20° and 45°) in Fig. 14. The change of the pitch angle close to the transition radius $R_t \approx 5''$ is quite obvious. There is an indication that the pitch angle is rising again after its drop at the transition radius, as expected from the

¹Englmaier & Shlosman (2000) define the radius where the shock front crosses the bar major axis for the first time as the transition radius R_t . Below this radius the gas density wave is driving the gas structure and forms a grand-design spiral structure.

model of a nuclear gas density wave. Note that in Fig. 13 we show the pitch angle of the northern spiral only, and its morphology strongly deviates from the dust and UV continuum morphology inside of the transition radius (see Section 4.1). It bends almost directly towards the nucleus, while the dust and UV continuum appear to form a ring. We will return to this discrepancy in Section 6.

Assuming that the indicated rise is real, the measured value of the pitch angle is higher than in the model by Englmaier & Shlosman (2000). It may be due to the fact that the inner spiral is beyond the linear regime explored in that model. The primary bar of NGC 4303 is stronger than the one in the model, and it may generate a stronger large-scale shock, which even in the central parts cannot be approximated by the linear wave theory, as in the spiral-shock model by Maciejewski et al. (2002).

6. LINKING ^{12}CO TO HST DATA: DYNAMICS AND MORPHOLOGY IN THE INNERMOST 500 PC

As shown in the previous section, Englmaier & Shlosman’s (2000) models of gas flow in a single bar are in a good agreement with the observed molecular gas behavior in the inner kiloparsec of NGC 4303 down to the 2-arcsec beam size of our data. The dynamics in this region can therefore be already well described by a model of a single bar with an ILR. In particular, we do not detect any strong inflowing motions throughout the whole inner bar, which would be characteristic for a *gaseous* inner bar as postulated by Shlosman et al. (1989). However, a secondary or inner, likely stellar, bar of $\sim 4''$ length is clearly present in the HST H band image (e.g Fig. 10). Due to its small size the use of our ^{12}CO data to search for inflow inside the inner bar is limited. Nevertheless, we can use the morphological information of the high resolution HST images ($\sim 0.2''$) to shed more light on the smaller-scale gas morphology in the presence of the secondary bar.

In the inner $4''$ the ^{12}CO morphology diverges from that seen in UV and traced by dust lanes (see section 4.1). To examine the behavior of the three tracers (CO, UV, and dust), we plot the distance from the nucleus as a function of the position angle in the inner kiloparsec for all of them (Fig. 13). For $\text{PA} = 330^\circ$ and 345° the parameters of the two dust lanes (described in Section 4.1), are given. The weaker dust lane follows the ^{12}CO pattern, while the more prominent lane joins the nuclear UV ring at $\text{PA} = 0^\circ$. The UV continuum forms almost a ring, as it is evident from the constant radius. Its geometry only deviates from a ring for position angles of $\geq 250^\circ$, where the string of UV-emitting regions seems to curl towards the center. The derived UV pitch angle oscillates around 20° , and does not show the rapid rise inwards as observed for the pitch angle of the ^{12}CO spiral.

Two interpretations of the UV images and the $V - H$ color maps seem plausible, and are discussed in detail below: (A) The UV continuum forms a nuclear ring which is extinguished north of the nucleus. This ring could then be related to gas dynamics expected in a double barred system. (B) The UV continuum forms a single-arm spiral. In this scenario, the inner bar might not at all affect the gas dynamics. In order to distinguish between the two scenarios, kinematic data of higher angular resolution are crucial.

6.1. Scenario (A): A nuclear ring

The outer UV continuum sources form a ring, onto which the ^{12}CO spiral converges, as seen in the transition from ^{12}CO ($\text{PA} \geq 200^\circ$) through dust ($250^\circ \leq \text{PA} \leq 360^\circ$) to UV ($\text{PA} \geq 0^\circ$) in Fig. 13. Here we show that the ring morphology is consistent with gas flow around a dynamically possible *stellar* secondary bar.

Dynamical constraints on double barred galaxies: A fixed relative position of two stellar bars cannot be stable for a long time, unless they remain parallel or orthogonal to each other (see e.g. Friedli 1996). The deprojected relative angle between the two bars in NGC 4303 is $\sim 30^\circ$, and thus the bars most likely do rotate with respect to each other. In numerical simulations of Friedli & Martinet (1993) and Rautiainen & Salo (1999) the two bars decouple dynamically, and may survive for long times, so that they can be treated as stable, long-lived systems. The presence of a moderate ILR of the primary bar is essential for the decoupling. Maciejewski & Sparke (2000) performed a search for orbits supporting bars within bars, and found that orbits supporting the inner bar originate from the x_2 orbits of the outer bar, and therefore the inner bar should form inside the ILR of the outer one. Maciejewski & Sparke (2000) were the first ones who postulated that straight shocks or dust lanes in the secondary bar are unlikely, because the orbital structure forces the secondary bar to end well inside its corotation. In such a bar, oval rings are expected instead of straight shocks. This finding was confirmed by hydrodynamic modeling by Maciejewski et al. (2002), which shows that the main effect of the secondary bar is to widen the nuclear ring created by the single bar. This ring evolves into an ellipse which rotates with the inner bar.

The morphology in the inner 500 pc: The distance between the straight gas lanes in the primary bar of NGC 4303 is much larger than the size of the inner bar, which differs from the modeled setup (Maciejewski et al. 2002). This allows the molecular gas spiral generated by the large-scale shock in the main bar to propagate considerably inwards before entering the region dominated by the secondary bar. Contrary to the model, the straight gas lanes in the main bar reach directly to the region dominated by the secondary bar. This difference may explain why the molecular gas in NGC 4303 forms a spiral outside the

inner bar. The innermost morphology, where the UV continuum forms a ring, is consistent with the model that predicts no straight shocks along the inner bar. However, one observed feature contradicts the model: a string of UV regions, which lies almost north of the nucleus (indicated by the arrow in Fig. 10; see also Fig. 2 of Colina & Wada 2000), coincides with the leading edge of the northern half of the secondary bar. These UV regions may indicate a shock along the inner bar that is not prohibitive to star formation. Thus, this secondary bar which is smaller than the one in the models of Maciejewski et al. (2002) can not only form a ring around itself, but it may also generate gas flows similar to those seen in the main bar, and, therefore, it might enhance gas inflow to the galactic center along the string of UV regions. If this is so, it is baffling to see no counterpart of this string on the other side of the bar, especially since the UV regions in the ring are more profound south of the nucleus.

Does NGC 4303 have an inner ILR? In Maciejewski & Sparke’s (2000) model, the inner bar cannot form inside the inner ILR of the main bar, since the x_2 orbits which are vital for its support do not extend there. In NGC 4303, the secondary bar is relatively smaller, and a direct calculation of gradients from measured points of the inner rotation curve gives a position of the iILR almost coinciding with the inner bar’s semi-major axis. If this is true, the secondary bar in this galaxy is *not* made out of equivalents of the x_2 orbits in the outer bar, and gas morphology and dynamics around it cannot be compared to the model above. However, the measured inner rotation curve should be treated with caution, as we are not sensitive to variations in velocity gradient of the inner 4” due to the resolution of the ^{12}CO data. As a result, one gets a rotation curve with almost linear growth for the innermost measured points. A linear rotation curve generates an angular frequency curve $\Omega - \kappa/2$ equal identically to zero, and unavoidably creates an artificial inner ILR. Based on our molecular data, a linear inner rotation curve cannot be distinguished from a non-linear rotation curve, which has an $\Omega - \kappa/2$ frequency diverging monotonically to infinity at small radii, and therefore no inner ILR. Thus NGC 4303 may not have an iILR at all, which justifies comparing it to the models of Maciejewski et al. (2002).

6.2. Scenario (B): A self-gravitating $m = 1$ mode? - Formation of a spiral

The morphology of the UV sources can also be interpreted as lined up along a single-arm spiral extending all the way to the galactic center. In this scenario the effect of the inner bar onto the gas flow would be negligible. As shown in section 4.1, the morphology of the star-forming UV clusters in NGC 4303 can be interpreted as a continuation of the northern ^{12}CO spiral arm. As there is no obvious spiral counterpart originating from the southern ^{12}CO arm, the UV clusters appear to be arranged into an $m = 1$ mode propagating

to the galaxy center. Such lopsidedness is not only detected on large scales but also in the central parts of spiral galaxies such as NGC 1808 (Emsellem et al. 2001) and NGC 3504 (Emsellem 2001). Moreover, single-arm nuclear spirals appear to be quite common in recent high-contrast observations (Martini 2001, Pogge & Martini 2002).

No prominent deviations in the residual ^{12}CO velocity field in the inner $8''$ of NGC 4303 (Fig. 9) can be associated with the UV structure, in contrast to the cases of NGC 1808 and NGC 3504, where the $m = 1$ modes are associated with clear kinematic signatures (Emsellem 2001). In NGC 4303, the appearance of the southern ^{12}CO spiral arm is distorted, but this asymmetry in the gas is probably too weak to display a kinematic signature. If this $m = 1$ mode is real, it underlines the importance of self-gravity for the gas component in the central region of NGC 4303: The induced and non-self-gravitating $m = 1$ mode cannot propagate in nuclear regions (Maciejewski et al. 2002).

Alternatively, the $m = 1$ mode may be only a transient feature created by a single sheared GMC. In Section 4.1, we showed that one of the more massive GMCs detected in ^{12}CO might already be able to form all the UV clusters. Consider a GMC originating from the northern arm: It gets sheared while spiraling into the galactic center, with star formation being triggered in separated parts at separate times. The dynamical time at a radius of $2.5''$ (~ 200 pc) is 10 Myr. The deprojected angle between the northern spiral arm and the western UV knots is about 120° , which corresponds to a time of ~ 4 Myr, consistent with the ages derived by Colina & Wada (2000). The ages of ~ 10 Myr for the eastern knots are similar to the travel time of ~ 8 Myr, if one assumes that the onset of star formation was delayed. As pointed out in Section 3.2, the stellar and molecular gas kinematics might not be the same, and, therefore, the stellar angular velocity might be lower, resulting in higher ages. However, in order to test this hypothesis good knowledge of the stellar kinematics in the inner $6''$ as well as age-dating of the individual clusters are essential.

6.3. Implications for the "bars-within-bars" scenario

In NGC 4303 molecular gas is found (within our spatial resolution) up to the very nucleus suggesting the presence of a mechanism transporting the gas down to small radii. However, the nature of this mechanism is not clear, as the combination of the ^{12}CO data with the HST data is consistent with two very different scenarios for the stellar and the gas component as discussed in the previous sections. The possible interpretations of our data leave the question about the importance of the inner bar for the gas flow towards the center unanswered. If the molecular gas forms a self-gravitating $m = 1$ mode or the observed spiral arm is a transient phenomenon, the inner bar is not important for the fueling of the

nucleus. *Gaseous* inner bars as postulated by Shlosman et al. (1989) are characterized by strong inflowing motions throughout the bar, and the ^{12}CO emission being aligned with the bar. Since neither of these are observed, this scenario has to be rejected. We also find some inconsistency with the predicted gas flow in stellar double bars: Some UV continuum emission coincides with the leading side of the inner bar on the scales of the HST resolution. This suggests that on this smaller scale, the inner bar in NGC 4303 may enable gas inflow, contrary to the results of the hydrodynamic model by Maciejewski et al. (2002). Compared to the modeled bars, the primary bar in NGC 4303 has a stronger potential which should offset the interaction between the two bars. Also the ratio of the bar lengths is at the upper end of that observed for double barred galaxies. This might be expected, since the stronger primary bar may allow only smaller secondary bars to form within it. These changes to the potential are likely to alter the gas flow. Dynamical models exploring a variety of double barred galaxies as well as more high-resolution observations of double barred galaxies are essential to better understand the fueling process on scales of a few 10 pc.

7. BEYOND DYNAMICAL MODELS

7.1. The asymmetry of the observed gas distribution

The gas leaving the straight shock in hydrodynamic models at the region where the shock starts to curl enters the diverging ‘spray’ flow towards the other shock (e.g. Fig. 8 and 9 of Regan et al. 1999). This behavior reinforces the bisymmetry of the flow, and smears out effects of global density variations.

As discussed in Section 3, the morphology as well as the intensity distribution of the ^{12}CO line emission is not completely point-symmetric. The western gas lane is about a factor of 1.8 brighter and therefore more massive than the eastern gas lane. Since we are only detecting about 40% of the total molecular gas in the inner arcminute (see Section 3), one possible explanation might be that the asymmetry in intensity is reflecting global density variations in the now-disturbed molecular gas disk. The mass/intensity ratio between the northern and southern gas spiral arm is about 1.6 if the nuclear emission is added to the northern spiral (assuming this emission is a continuation of the northern spiral, see Section 5). The clump about $3''$ to the south-east of the nucleus, between the eastern gas lane and the southern spiral arm, could then be a result of that asymmetry: dense material from the western gas lane enters the ‘spray’ region there, and is more visible than its counterpart from the eastern lane. The time scale for molecular gas to travel from the western gas lane to the eastern one at the radius of $4 - 8''$ (310 – 620 pc) can be estimated by assuming that the rotation velocity is a good measure of the net circular velocity in this region. We find

that it takes only about 5 – 10 Myr. This would imply that the global density variations were either very strong in the beginning and the bar potential is still trying to smooth them out, or that the torque of the bar onto the molecular gas disk has only started, i.e. the bar has only formed recently. Because of the large amount of missing flux we favor the second possibility.

7.2. The role of star formation

Most dynamical models do not include star formation and its effects like supernova explosions and stellar winds. Therefore they might miss a critical component for the gas dynamics in the inner kiloparsec of barred galaxies (e.g. Sheth et al. 2000). NGC 4303 offers the possibility to explore the importance of these effects, as it hosts young stellar clusters in addition to molecular gas. We neglect the consumption of molecular gas during star formation, since this effect is smaller than changes in kinematics resulting from outflows from young stars.

The molecular gas geometry in the inner 8'' of NGC 4303 is disturbed, and shows no tight spatial correlation with the star formation. This is in contrast to observations of other starburst rings such as the one in NGC 4314 (Benedict et al. 1996). Although NGC 4303 is in a tidal interaction with two nearby companions (NGC 4292 and NGC 4303A, Binggeli et al. 1985), it is very likely that the gravitational potential of NGC 4303 dominates the inner kiloparsec. As outlined in section 7.1, there is no obvious reason for the asymmetry from a dynamical point of view. One possibility might be the impact of massive star formation via stellar winds and supernovae explosions which will be discussed below.

7.2.1. The star formation threshold in the ILR region

As shown in Section 4.1 the UV continuum lies in the region of the molecular gas spiral arms, and between the inner and outer ILR (see section 4.3). Elmegreen (1994) used a linear instability analysis to estimate the critical density for star formation within the inner Lindblad resonance (ILR). Since it is possible to measure the gas density in NGC 4303 in the presence of star formation, we can compare the observations to theoretical predictions. The critical density ρ_{crit} can be approximated with $\rho_{crit} = 0.6\kappa^2 G^{-1}$, where κ is the epicyclic frequency. Using our values for $\kappa(3'') \sim 1050 \text{ km s}^{-1} \text{ kpc}^{-1}$ at the distance of the UV ring of $r \sim 225 \text{ pc}$, we get a critical density $\rho_{crit} \approx 140 \text{ M}_{\odot} \text{ pc}^{-3}$. The observed molecular hydrogen mass is $\sim 3.5 \times 10^7 \text{ M}_{\odot}$. Assuming a ring with a width of about 1'' (78 pc) at a radius of 225 pc

and a gas disk scale height of 30 pc (see Section 3), we find a gas density of $\sim 10 \text{ M}_\odot \text{ pc}^{-3}$ for the position of the UV ring. This is only about a factor of 15 lower than the critical density, similar to the high critical density found for the starburst ring in M 82 (Wild et al. 1992). However, since the width of the ring is not resolved in our ^{12}CO data, the gas density has to be regarded as a lower limit. Making the ring thinner by a factor of two, similar to the dust features seen in the HST $V - H$ color map, and correcting the molecular gas mass for the Helium contribution (36% of the molecular gas mass) brings the gas density close enough to the critical density to explain the presence of the UV starburst ring.

7.2.2. Feedback of the star formation onto the ISM

As pointed out in Section 4.1 the young stellar clusters might have affected the distribution of the molecular gas by the impact of stellar winds and supernovae explosions. A simple energy estimate can be used to test if such a large redistribution of the interstellar medium due to stellar winds and SNe can be responsible for the disturbed ^{12}CO distribution in the central kiloparsec of NGC 4303.

The mechanical luminosity (of stellar winds and supernovae) of a 10^6 M_\odot stellar cluster is about $10^{39.5} \text{ erg s}^{-1}$ during the first few Myr regardless if the star formation is instantaneous or continuous (e.g. STARBURST99; Leitherer et al. 1999). Therefore the average stellar cluster in NGC 4303 with a stellar mass of $0.7 \times 10^5 \text{ M}_\odot$ has released a mechanical energy of about $3.8 \times 10^{52} \text{ erg}$ ($1.1 \times 10^{53} \text{ erg}$) into the interstellar medium after 6 Myr (17 Myr). This is equivalent to 38 (110) Type II SNe per stellar cluster.

If the observed molecular gas did coincide with the sites of the stellar clusters at a radius of $r_{UV} \sim 3''$ (230 pc) at a former time, then in order to push it to its present location at a radius of $r_{GMC} \sim 4''$ (310 pc) its potential and kinetic energy have to be increased. Under the assumption that the gravitational potential can be approximated by a spherically symmetric mass distribution, the gain in potential energy is

$$\Delta E_{pot} = m_{GMC} \int_{r_{UV}}^{r_{GMC}} \frac{v_{circ}^2(r)}{r} dr. \quad (1)$$

An average cloud of molecular gas in the southern spiral arm has a mass of $m_{GMC} \sim 5 \times 10^6 \text{ M}_\odot$ (see Section 4.1), the velocity at the position of the UV ring and the southern GMCs are $v(r_{UV} = 3'') \approx 137 \text{ km s}^{-1}$ and $v(r_{GMC} = 4'') \approx 150 \text{ km s}^{-1}$, respectively. Integration over the circular velocities v_{circ} taken directly from the measured rotation curve (Fig.8) results in the acquired potential energy of $\Delta E_{pot} \sim 9 \times 10^{53} \text{ erg}$. At the same time, this cloud of

molecular gas will have to gain the kinetic energy

$$\Delta E_{kin} = m_{GMC} \frac{v(r_{GMC})^2 - v(r_{UV})^2}{2} \approx 2 \times 10^{53} \text{ erg} \quad (2)$$

Thus the total energy needed to move the molecular gas cloud outwards from $r_{UV} = 3''$ to $r_{GMC} = 4''$ is the sum of the increment in potential energy ΔE_{kin} needed to get out of the potential well, and the increase in kinetic energy ΔE_{kin} on the rising part of the rotation curve. Together these amount to at least $\sim 10^{54}$ erg.

This value is already considerably larger than the mechanical energy released by a single stellar cluster during its lifetime. In addition, most of the mechanical energy heats up the gas, and we did not take into account these radiative losses. Thus the realistic estimate of energy needed to push a single molecular cloud out from $3''$ to $4''$ is even much higher than $\sim 10^{54}$ erg; it therefore seems very unlikely that the UV clusters seen south of the nucleus have altered the southern CO spiral arm.

However, a different effect might be important for changing the apparent gas distribution. Weiß et al. (2001) have shown in M 82 that the excitation conditions for the molecular lines can differ in the presence of massive star formation: The molecular gas appears brighter than the surrounding gas which has lower temperatures, thus suggesting a different geometry. A multi-transition study of the molecular gas is needed to test if a similar scenario with varying excitation conditions can explain the observed asymmetry in NGC 4303. This highlights the fact that it is essential to better understand the physical interplay between the molecular gas properties and massive star formation occurring in the inner kiloparsec of double-barred galaxies.

7.3. A forming starburst ring in NGC 4303?

The striking difference in the molecular gas morphology of NGC 4303 compared to other double barred galaxies such as NGC 4314 (Benedict et al. 1996) or NGC 1068 (Schinnerer et al. 2000a) is the fact that the bulk of the molecular gas is located in the gas lanes, and not in the star-forming ring. This might indicate that the circumnuclear region in NGC 4303 is in an early state of evolution. Another difference is the appearance of the ring: NGC 4314 and NGC 1068 both show almost circular tightly wound spirals resembling a ring whereas the molecular gas in NGC 4303 forms a grand design spiral pattern. In addition, the off-nuclear star formation coincides with the gas rings in NGC 4314 and NGC 1068 suggesting that the stars have formed within the gas rings. This is in agreement with the assumption that these rings might be older than the one in NGC 4303. Therefore, the spiral structure seen in the UV continuum in NGC 4303 might evolve into a ring as well, similar to those observed in

NGC 4314 and NGC 1068. In this case, on-going star formation is expected to last for a longer time than a few million years within the ring. This would be in agreement with the finding of Maoz et al. (2001) who argued for a constant star formation of about 200 Myr in the two starburst rings they analyzed.

8. SUMMARY AND CONCLUSION

NGC 4303 is one of the first double barred galaxies in which the molecular gas properties can be studied in detail at high angular and spectral resolution. The primary bar in NGC 4303 has a typical length of about 6 kpc whereas the inner bar is considerably smaller, with a length of about 340 pc. There is a surprisingly good agreement between the observed overall gas geometry and dynamical models for the gas flow in barred galaxies.

We detect only about 40% of the single-dish flux in our interferometric map, indicating that there is still a large smooth reservoir of molecular gas in the inner arcminute of NGC 4303. The gas forms two straight lanes where deviations of up to 90 km s^{-1} from the mean rotational velocity are observed. In the context of hydrodynamic models this behavior can be explained as inflowing motions in the large-scale bar. The velocity field of the inner $8''$ is consistent with a circular rotating disk and shows deviations of only $\sim 5 - 15 \text{ km s}^{-1}$. The bulk of the molecular gas is found in the gas lanes and not in the nuclear region. This may indicate that the circumnuclear molecular gas is still settling into the typical ring-like configuration, and that the star forming ring in NGC 4303 is still young.

The star-forming ring analyzed by Colina et al. (1997, 1999) has no direct counterpart in the molecular gas distribution. The critical density for star formation in the UV ring region (region of the ILR) is only about ~ 15 times higher than the estimated gas density. Therefore it seems plausible that the circumnuclear star formation was started due to the gas inflow triggered by the primary bar. The disturbed geometry of the southern gas spiral arm suggests that the massive star formation has affected the molecular gas distribution. However, a simple energy estimate suggests that the mechanical energy produced by the stellar clusters is too low to overcome the gravitational potential.

There is no strong correlation between the extinction as seen in the HST $V - H$ map and the distribution of the molecular gas. Possible reasons are that the light is dominated by different stellar populations as well as that an ionization cone might have affected the distribution of extinguishing material.

The overall morphology of the molecular gas resembles closely the predicted gas distribution in dynamical models of strongly barred galaxies. In the inner kiloparsec the gas

lanes start to curl and form a spiral structure which is distorted in the southern spiral arm. Detailed comparison between high resolution models of Englmaier & Shlosman (2000) and the ^{12}CO data of NGC 4303 for the inner kiloparsec shows that the observed spiral structure can be explained by the density wave generated in a large-scale bar. No strong inflowing motions characteristic for a secondary gaseous bar have been detected in our ^{12}CO data. After including the HST data in the analysis of the central 400 pc ($\sim 5''$) two scenarios seem plausible:

1. The innermost morphology observed with HST shows a nuclear ring inside of the nuclear ^{12}CO spiral: This is uncommon in a single bar, but consistent with the gas flows in a dynamically possible double bar model (Maciejewski et al. 2002). The large ratio (~ 15) between the two bar lengths in NGC 4303 is much larger than in this model, therefore there is room for the ^{12}CO spiral structure to propagate inwards before it enters the region dominated by the secondary bar. The faint UV emission present at the leading side of the inner bar might indicate inflow of gas along the inner bar.
2. The UV continuum traces an $m = 1$ spiral mode which is self-gravitating, and propagates independently of the inner bar.

It is imperative to study more double barred systems at high angular resolution to investigate the fueling of the central few parsecs. Also, dynamical models of double barred galaxies covering a wide range of different properties such as primary bar strength, and varying bar length ratios are important in order to better understand the gas flow in these systems.

This study has shown that the overall gas flow in NGC 4303 is dominated by the large-scale bar, and very reminiscent of current dynamical models. However, the observed asymmetry in the gas distribution in NGC 4303 cannot be explained in detail with current models. Also, the impact of star formation and feedback on the ISM inside the ILR may be quite significant, and needs further consideration. NGC 4303 obviously offers an important example against which to test elaborate models, though it will be interesting to see with comparable observations of other double barred galaxies whether it is unique, or whether it is representative of a broader class of galaxies.

It is a pleasure to thank P. Englmaier, P. Erwin and E. Emsellem for stimulating discussions. ES acknowledges support by National Science Foundation grant AST 96-13717, and LAM was supported by the PPARC Rolling Grant PPA/G/O/1999/00193 at the University of Oxford. LAM is also thankful for partial support by NSF grant AST 96-13717 to

visit the California Institute of Technology as part of this work. Support of this work was also provided by a grant from the K. T. and E. L. Norris Foundation. Research with the Owens Valley Radio Telescope, operated by California Institute of Technology, is supported by NSF grant AST 96-13717. This research has made use of the NASA/IPAC Extragalactic Database (NED) which is operated by the Jet Propulsion Laboratory, California Institute of Technology, under contract with the National Aeronautics and Space Administration. We have made use of the LEDA database (<http://leda.univ-lyon1.fr>).

REFERENCES

- Athanassoula, E., 1992, MNRAS, 259, 345; (A92)
- Banfi, M., Rampazzo, R., Chincarini, G., Henry, R.B.C., 1993, A&A, 280, 373
- Benedict, G.F., Smith, B.J., Kenney, J.D.P., 1996, AJ, 112, 1318
- Binggeli, B., Sandage, A., Tammann, G.A., 1985, AJ, 90, 1681
- Buta, R., Crocker, D.A., 1993 AJ, 105, 1344
- Calzetti, D., Kinney, A. L., & Storchi-Bergmann, T. 1994, ApJ, 429, 582
- Cayatte, V., van Gorkom, J.H., Balkowski, C., Kotanyi, C., 1990, AJ, 100, 604
- Chapelon, S., Contini, T., Davoust, E., 1999, A&A, 345, 81
- Contopoulos, G., 1981, A&A, 102, 265
- Colina, L., Arribas, S., 1999, ApJ, 514, 637
- Colina, L., Garcia Vargas, M.L., Mas-Hesse, J.M., Alberdi, A., Krabbe, A., 1997, ApJ, 484, L41
- Colina, L., Wada, K., 2000, ApJ, 529, 845
- Combes, F., Becquaert, J-F., 1997, A&A, 326, 554
- Elmegreen, B.G., 1994, ApJ, 425, L73
- Elmegreen, B.G., Efremov, Y., Pudritz, R.E., Zinnecker, H. 1999, in "Protostars and Planets IV", Univ. of Arizona Press, p. 179
- Emsellem, E., 2001, in "The Central kpc of Starbursts and AGN", ed. J.H. Knapen, J.E. Beckman, I. Shlosman, & T.J. Mahoney, ASP Conf. Ser., 249, 91
- Emsellem, E., Greusard, D., Combes, F., Friedli, D., Leon, S., Pécontal, E., Wozniak, H. 2001, A&A, 368, 52
- Englmaier, P., Gerhard, O., 1997, MNRAS, 287, 57
- Englmaier, P., Shlosman, I., 2000, ApJ, 528, 677
- Erwin, P., Sparke, L.S. 2002, AJ, in press, astro-ph/0203514

- Ferrarese, L., et al. 1996, *ApJ*, 464, 568
- Frei, Z., Guhathakurta, P., Gunn, J.E., Tyson, J.A., 1996, *AJ*, 111, 174
- Friedli, D. 1996, *A&A*, 312, 761
- Friedli, D., Martinet, L., 1993, *A&A*, 277, 27
- Garcia, A.M., 1993, *A&ASuppl.*, 100, 47
- Genzel, R., Weitzel, L., Tacconi-Garman, M., Blietz, M., Krabbe, A., Lutz, D., Sternberg, A., 1995, *ApJ*, 444, 129
- Guhathakurta, P., van Gorkom, J.H., Kotanyi, C.G., Balkowski, C., 1988, *AJ*, 96, 851
- Heraudeau, Ph., Simien, F., 1998, *A&ASuppl.*, 133, 317
- Ho, L.C., Filippenko, A.V., Sargent, W.L.W., 1997, *ApJ*, 487, 591
- van der Hulst, J.M., Terlouw, J.P., Begeman, K., Zwitter, W., Roelfsema, P.R., in “Astronomical Data Analysis Software and Systems I”, eds. D. M. Worall, C. Biemesderfer and J. Barnes, ASP Conf. series no. 25, p. 131
- Jogee, S., Shlosman, I., Laine, S., Englmaier, P., Knapen, J.H., Scoville, N.Z., Wilson, C.D., 2002, *ApJ*, sub., astro-ph/0202270
- Jungwiert, B., Combes, F., Axon, D.J. 1997, *A&ASuppl.*, 125, 479
- Kenney, J.D., Young, J.S., 1988, *ApJS*, 66, 261
- Koopmann, R.A., Kenney, J.D.P., Young, J., 2001, *ApJS*, 135, 125
- Laine, S., Knapen, J.H., Pérez-Ramírez, D., Englmaier, P., Matthias, M. 2001, *MNRAS*, 324, 891
- Laine, S., Shlosman, I., Knapen, J.H., Peletier, R.F. 2002, *ApJ*, 567, 97
- Leitherer, C. et al. 1999, *ApJS*, 123, 3
- Ma, J., Peng, Q.-H., Gu, Q.-S., 1998, *A&ASuppl.*, 130, 449
- Maciejewski, W., Sparke, L.S., 1997, *ApJLetters*, 484, L117
- Maciejewski, W., Sparke, L.S., 2000, *MNRAS*, 313, 745
- Maciejewski, W., Teuben, P.J., Sparke, L.S., Stone, J.M. 2002, *MNRAS*, 329, 502

- Maoz, D., Barth, A.J., Ho, L.C., Sternberg, A., & Filippenko, A.V. 2001, *AJ*, 121, 3048
- Martin, P., 1995, *AJ*, 109, 2428
- Martini, P., 2001, in "The Central kpc of Starbursts and AGN", ed. J.H. Knapen, J.E. Beckman, I. Shlosman, & T.J. Mahoney, *ASP Conf. Ser.*, 249, 98
- Martini, P., Pogge, R.W. 1999, *AJ*, 118, 2646
- Meier, D.S., Turner, J.L., Hurt, R.L. 2000, *ApJ*, 531, 200
- Perez-Ramirez, D., Knapen, J.H., Peletier, R.F., Laine, S., Doyon, R., Nadeau, D., 2000, *MNRAS*, 317, 234
- Piner, B.G., Stone, J.M., Teuben, P.J., 1995, *ApJ*, 449, 508
- Pogge, R.W., Martini, P., 2002, *ApJ*, in press, astro-ph/0201185
- Quillen, A.C., De Zeeuw, P.T., Phinney, E.S., Phillips, T.G., 1992, *ApJ*, 391, 121
- Rautiainen, P., Salo, H. 1999, *A&A*, 348, 737
- Regan, M.W., Mulchaey, J.S., 1999, *AJ*, 117, 2676
- Regan, M.W., Sheth, K., Vogel, S.N., 1999, *ApJ*, 526, 97
- Rubin, V.C., Waterman, A.H., Kenney, J.D.P., 1999, *AJ*, 118, 236
- Sault, R.J., Teuben, P.J., Wright, M.C.H., 1995, in "Astronomical Data Analysis Software and Systems IV", ed. R. Shaw, H.E. Payne, J.J.E. Hayes, *ASP Conf. Ser.*, 77, 433
- Schinnerer, E., Eckart, A., Tacconi, L.J., 2000b, *ApJ*, 533, 850
- Schinnerer, E., Eckart, A., Tacconi, L.J., Genzel, R., Downes, D. 2000a, *ApJ*, 533, 850
- Schmitt, H.R., Kinney, A.I., 1996, *ApJ*, 463, 498
- Scoville, N.Z., Carlstrom, J.E., Chandler, C.J., Phillips, J.A., Scott, S.L., Tilanus, R.P.J., Wang, Z., 1993, *PASP*, 105, 1482
- Sheth, K., 2001, Ph.D. thesis, Univ. of Maryland
- Sheth, K., Regan, M. W., Vogel, S. N., & Teuben, P. J. 2000, *ApJ*, 532, 221
- Shlosman, I., Frank, J., Begelman, M.C. 1989, *Natur*, 338, 45

- Strong, A. W., et al. 1987, Proc. 20th Intern. Cosmic Ray Conf., I, 125
- Telesco. C.M., Becklin, E., Wynn-Williams, C., Harper. D., 1984, ApJ, 282, 427
- Wada, K., Norman, C.A., 1999, ApJ, 516, L13
- Warmels, R.H., 1988, A&ASuppl., 72, 57
- Wei, A., Neininger, Httemeister, S., Klein, U., 2001, A&A, 365, 571
- Wei, A., Walter, F., Neininger, N., Klein, U., 1999, A&A, 345, L23
- Wild, W., Harris, A.I., Eckart, A., Genzel, R., Graf, U.U., Jackson, J.M., Russell, A.P.G.,
Stutzki, J. 1992, A&A, 265, 447
- Young, J.S., et al., 1995, ApJS, 98, 219

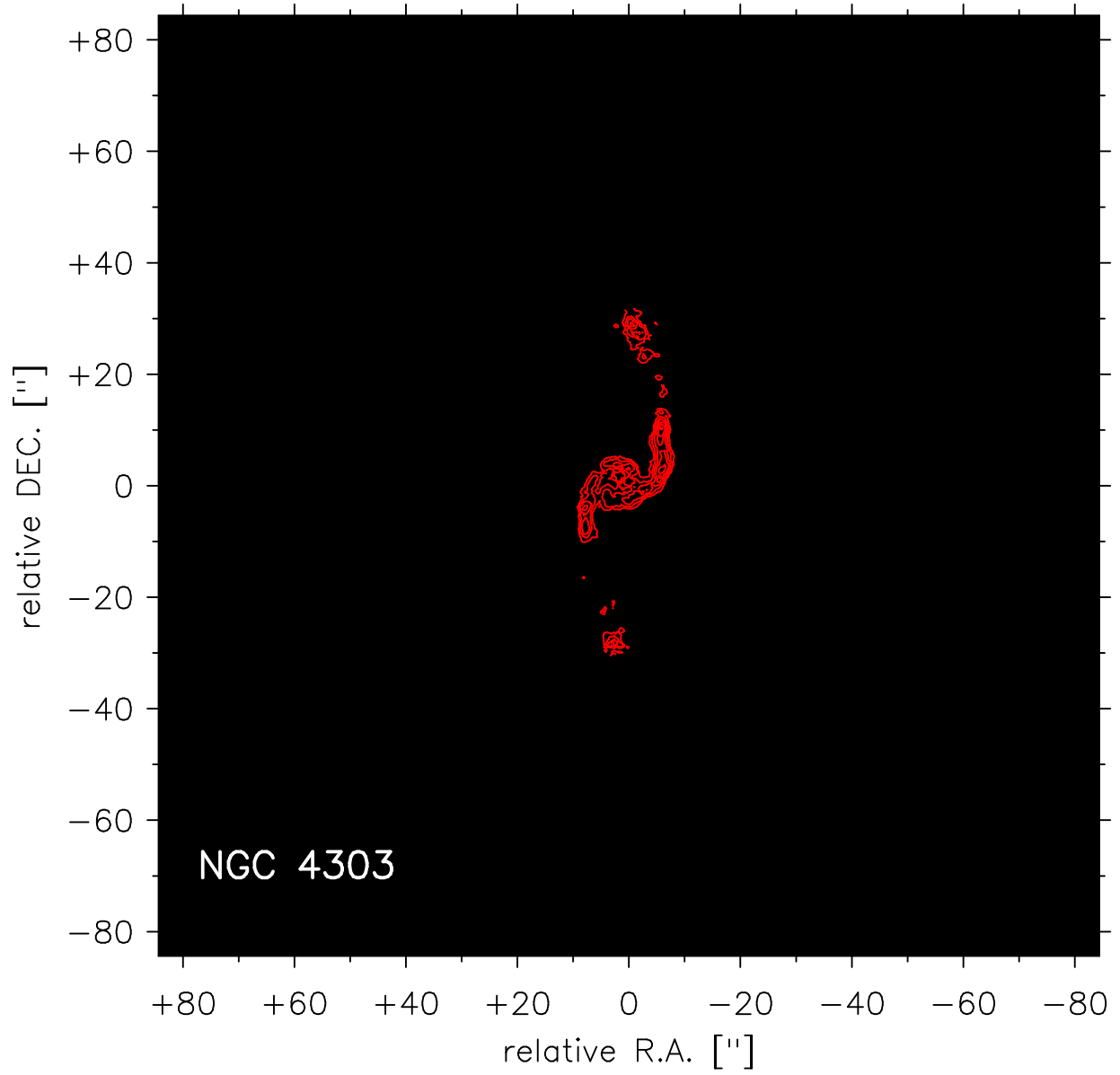


Fig. 1.— The ^{12}CO 1–0 emission (red contours; primary beam corrected) as observed with the OVRO mm-interferometer lies inside the prominent spirals seen in the i band image of Frei et al. (1996). Note, that there is also molecular emission associated with the spiral arms (see Sheth 2001).

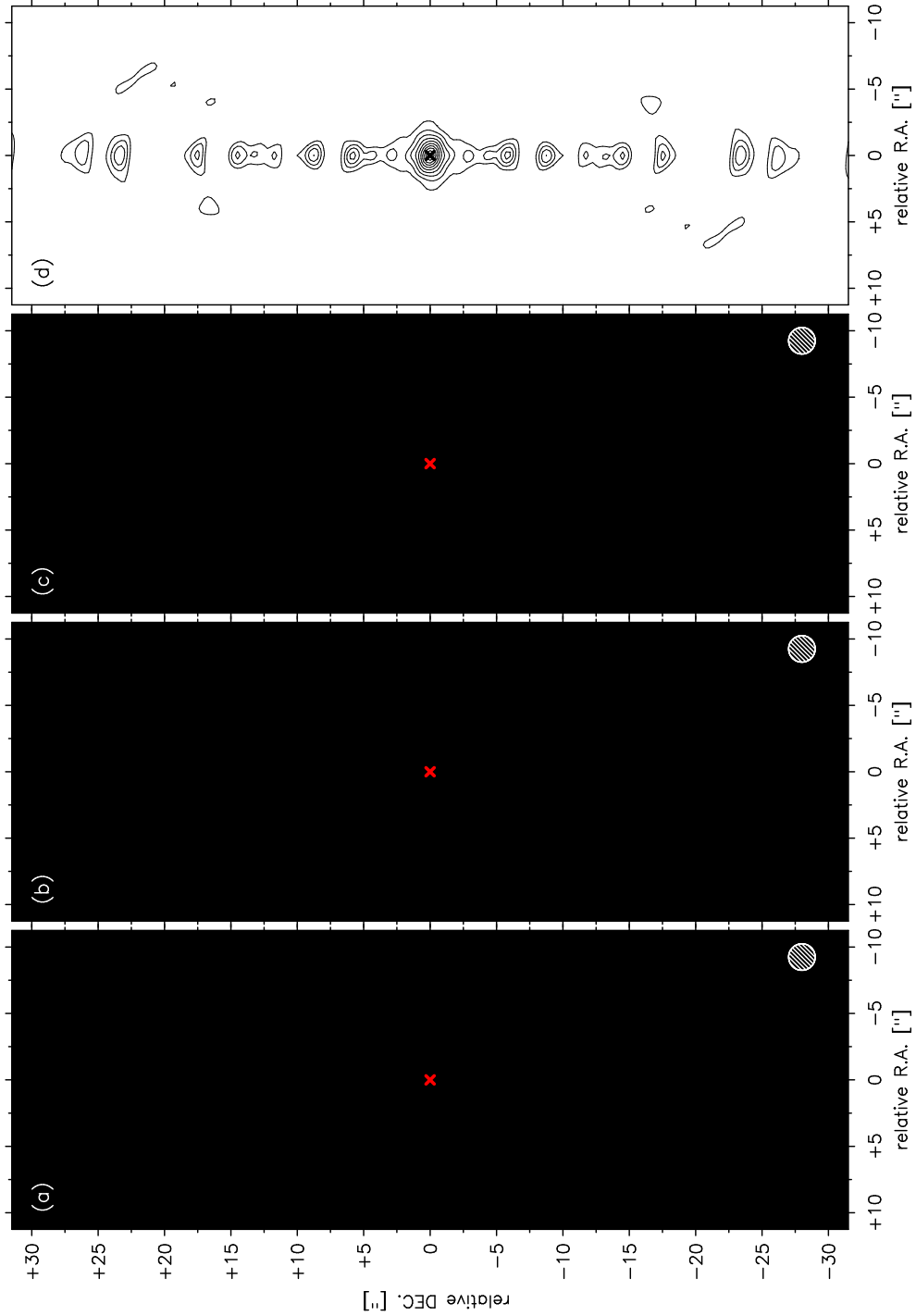


Fig. 2.— Moment maps of NGC 4303 from the OVRO mm-interferometer (primary beam corrected) $^{12}\text{CO } 1 - 0$ line data at a spatial resolution of $2.0''$. The offset coordinates refer to the derived dynamical center (see Table 2). (a) Intensity map (0th moment), (b) Velocity field (1st moment), and (c) Dispersion map (2nd moment). (d) The dirty beam is shown in contours of 10%, 20%, ... , 100%.

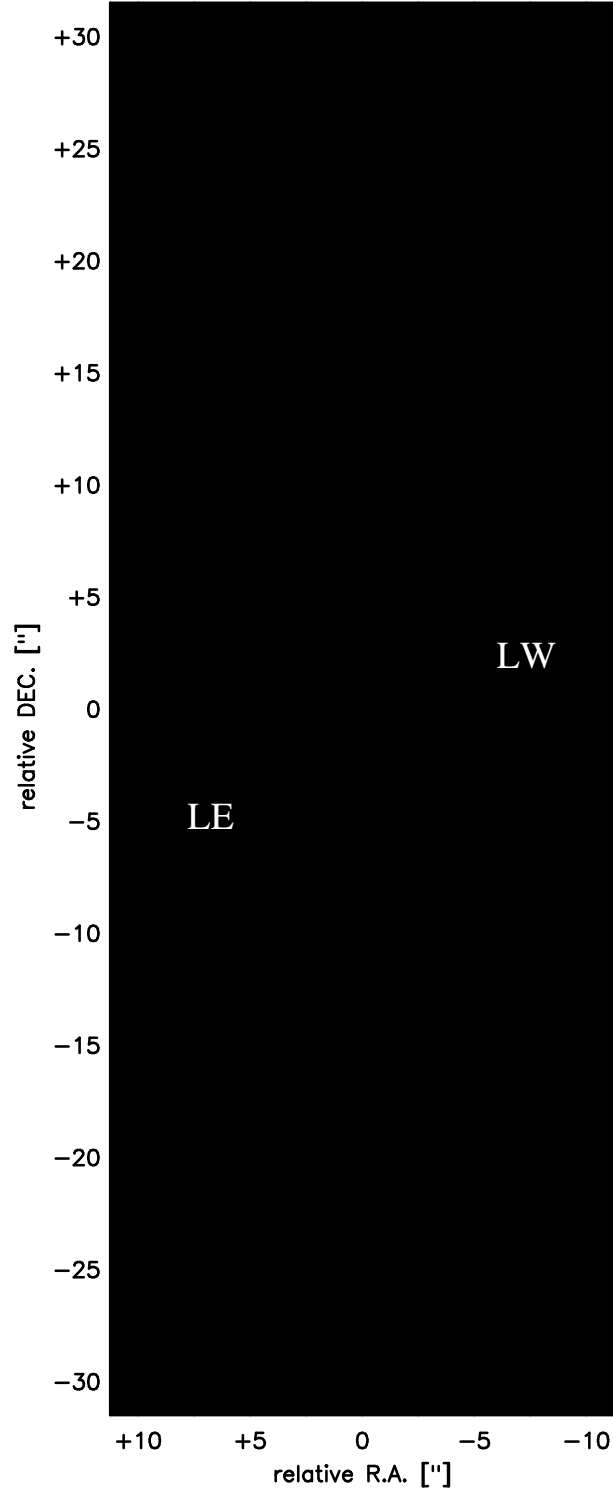


Fig. 3.— The individual components of the ^{12}CO line emission which are discussed in the text are indicated in the 0th moment map. (PN, PS, LE, LW, and N denote the position of the extracted spectra shown in Fig. 4.)

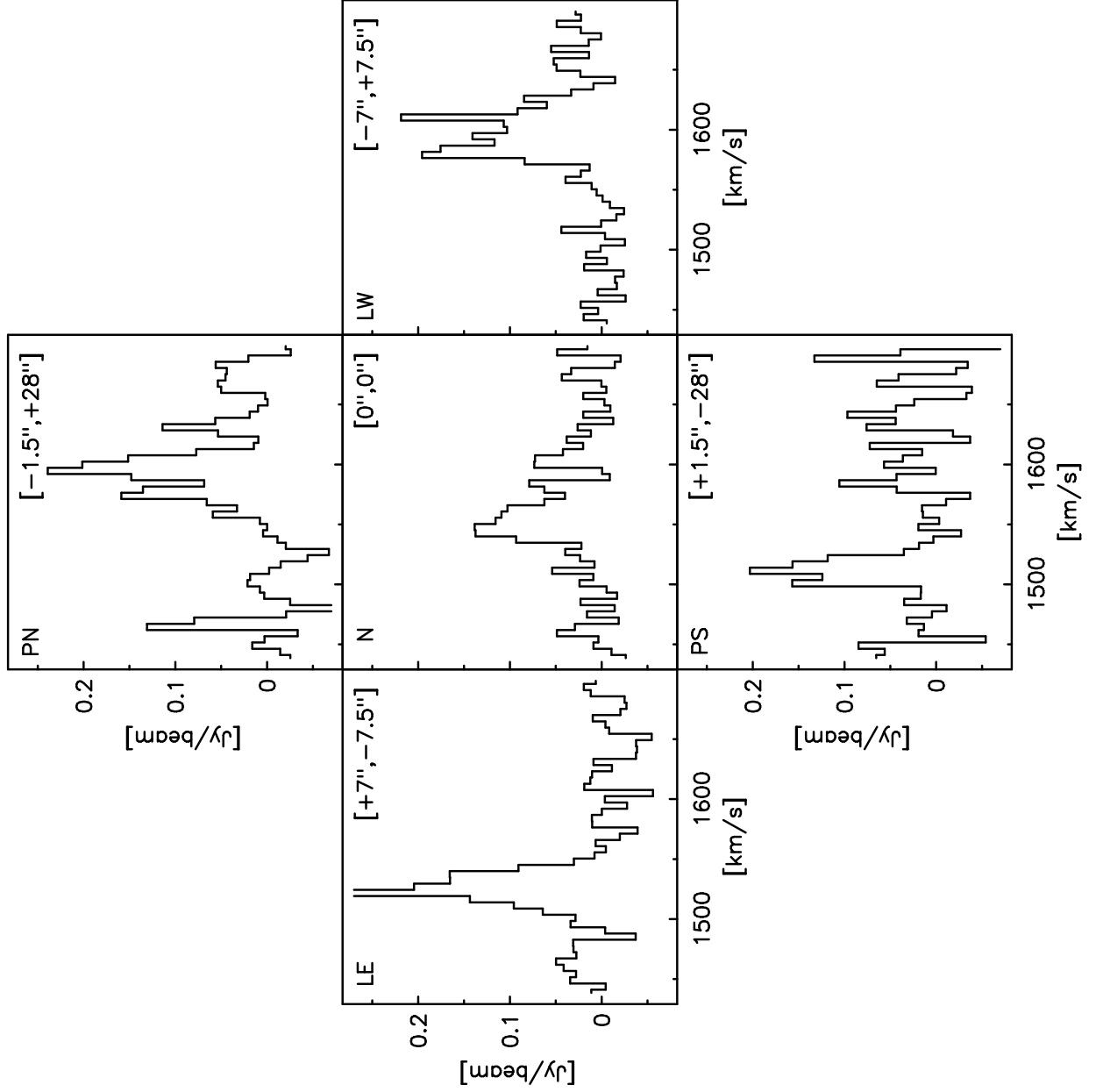


Fig. 4.— ^{12}CO $1-0$ line spectra extracted (from the primary beam corrected data) at the position of the nucleus, the emission peaks in the gas lanes, and the emission peaks near the bar ends. The line center is clearly shifting between the various positions. The positions of the spectra are indicated in Fig. 3.

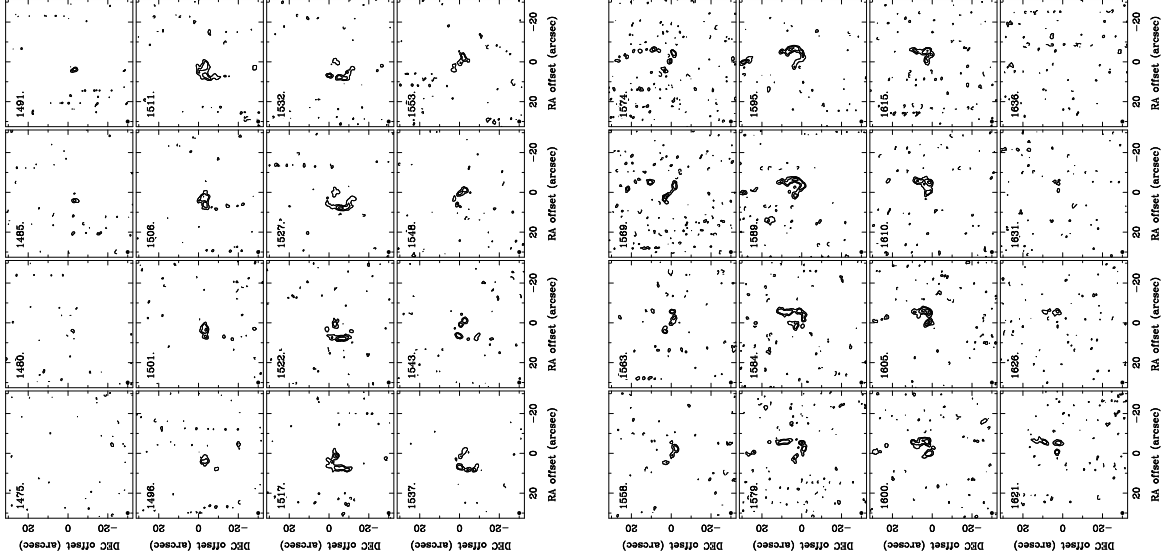


Fig. 5.— OVRO channel maps of the ^{12}CO $1-0$ line emission at a spatial resolution of $2.0''$. The contours are at $-3, 3, 5, 8, 11$, and 14σ with $1\sigma = 25 \text{ mJy beam}^{-1}$. The (LSR) velocity is given in each channel map.

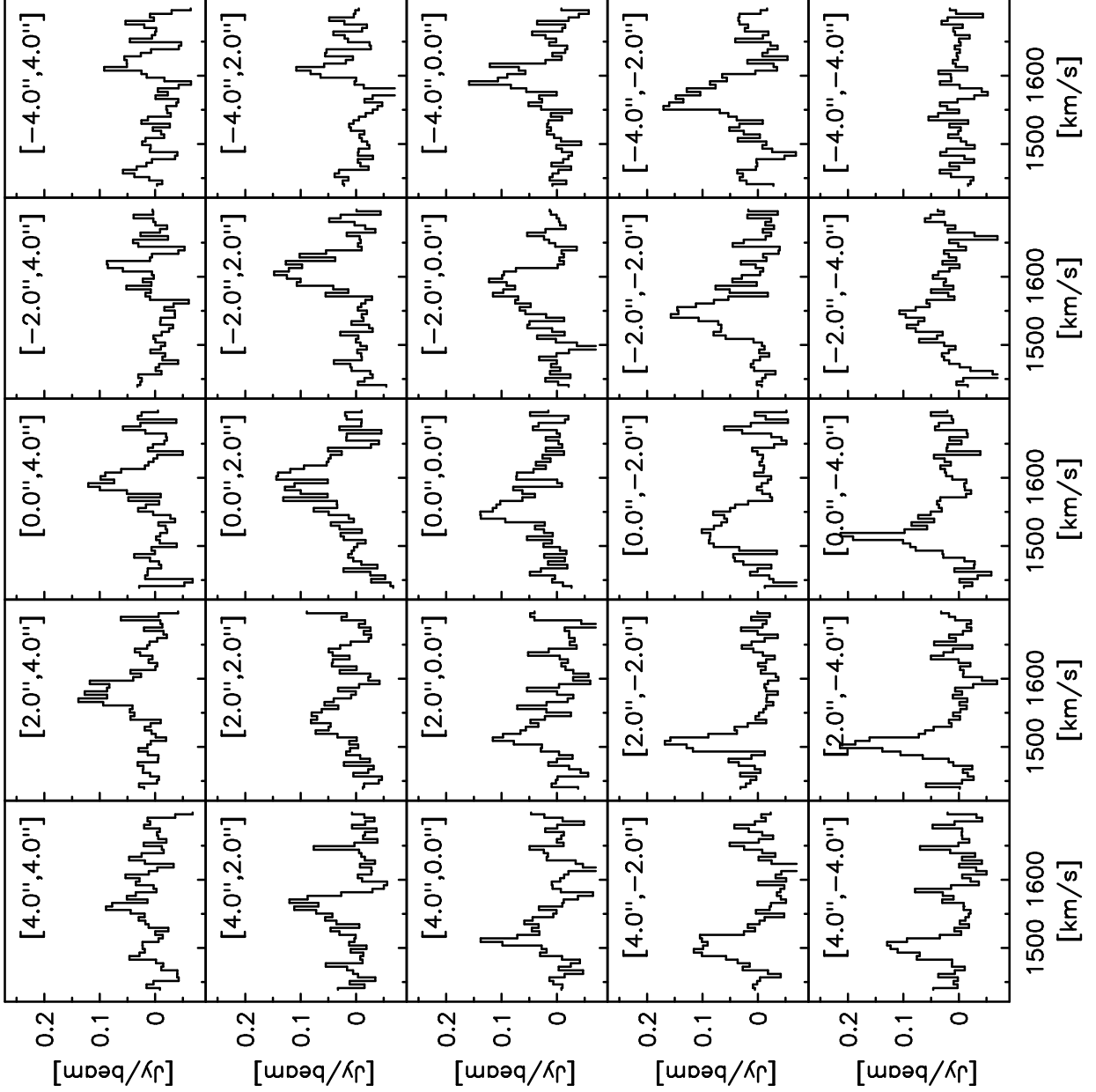


Fig. 6.— ^{12}CO $1 - 0$ line spectra extracted in the inner $8''$ in steps of $2''$. The spectra south-west of the nucleus show wider lines indicating the presence of a second component.

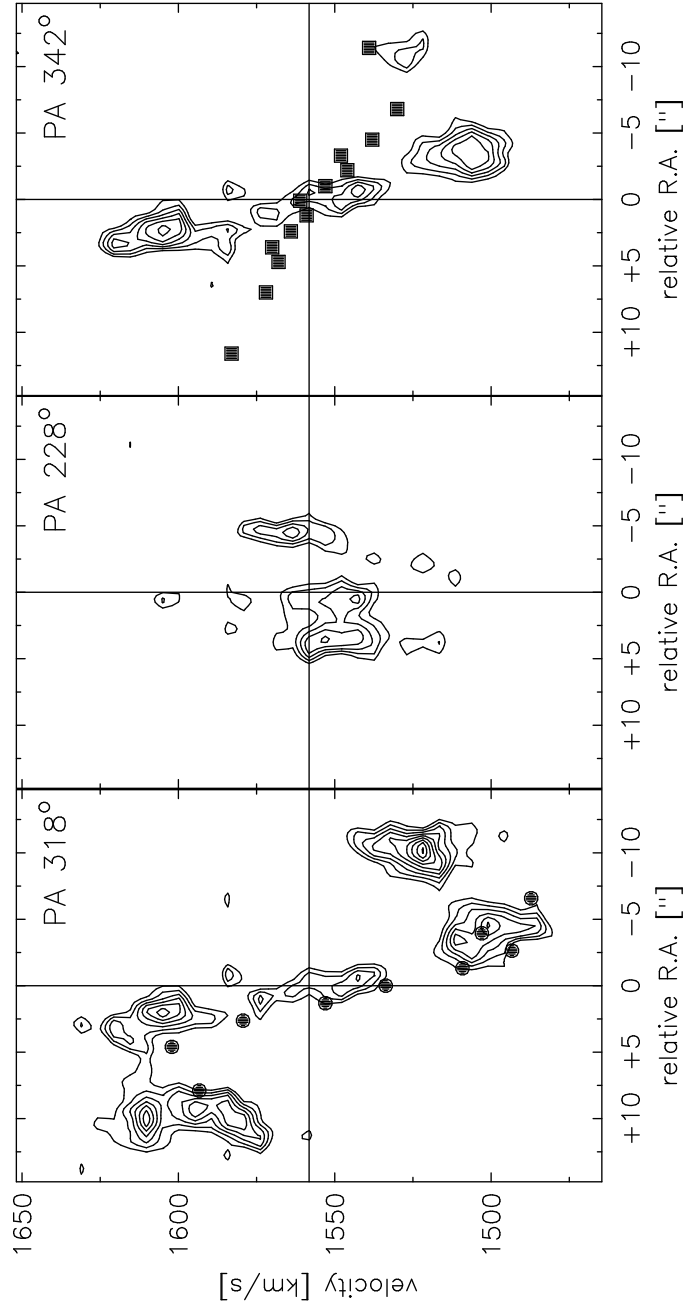


Fig. 7.— pv diagrams along the major (PA 318° ; *left*) and minor (PA 228° , *middle*) kinematic axis of the ^{12}CO 1 – 0 line emission at a spatial resolution of $2.0''$ and a spectral resolution of 5.2km s^{-1} . The filled points in the pv diagram at PA 318° are the $\text{H}\alpha$ measurements of Rubin et al. (1999). The pv diagram at PA 342° (*right*) shows in addition the stellar measurements of Heraudeau et al. (1998) in filled squares. The contours start at 3σ and are in steps of $1\sigma=25\text{ mJy beam}^{-1}$.

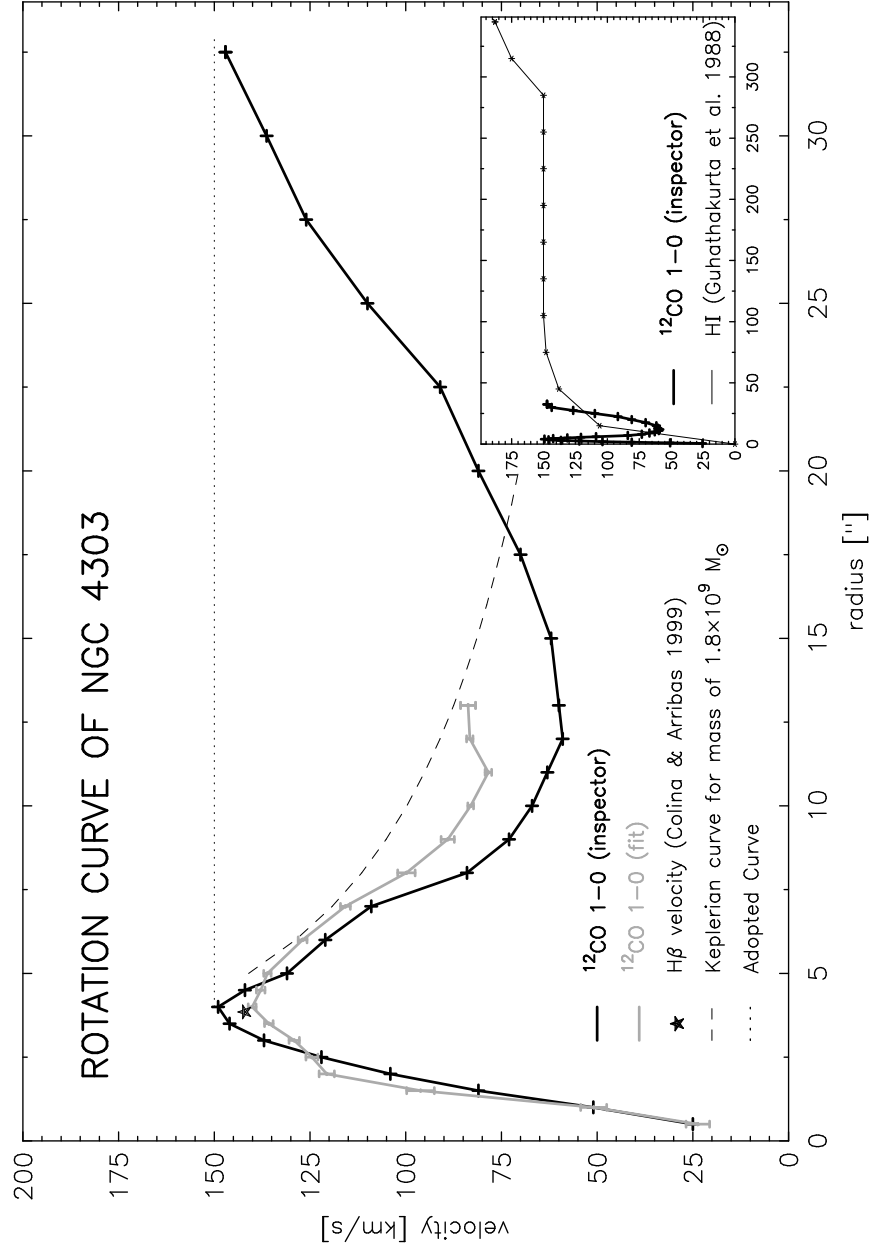


Fig. 8.— Derived rotation curve for NGC 4303. The results of the two different fitting routines for the $^{12}\text{CO } 1-0$ data are shown in fat lines (grey: ROTCUR; black: INSPECTOR). The derived rotation velocity of Colina & Arribas (1999) is given as well (star) after correcting for the difference in inclination. The broken line represents the Keplerian rotation velocity for a point mass of $1.8 \times 10^9 M_{\odot}$. The molecular gas rotation curve is clearly sub-Keplerian for radii between $r \sim 4'' - 18''$, strongly suggesting that non-circular motions dominate the molecular gas motion here. Therefore, we adopted a constant rotation velocity of 150 km s^{-1} for these radii (dotted line). The HI rotation curve of Guhathakurta et al. (1988) is shown for comparison in the inset. See text for further discussion.

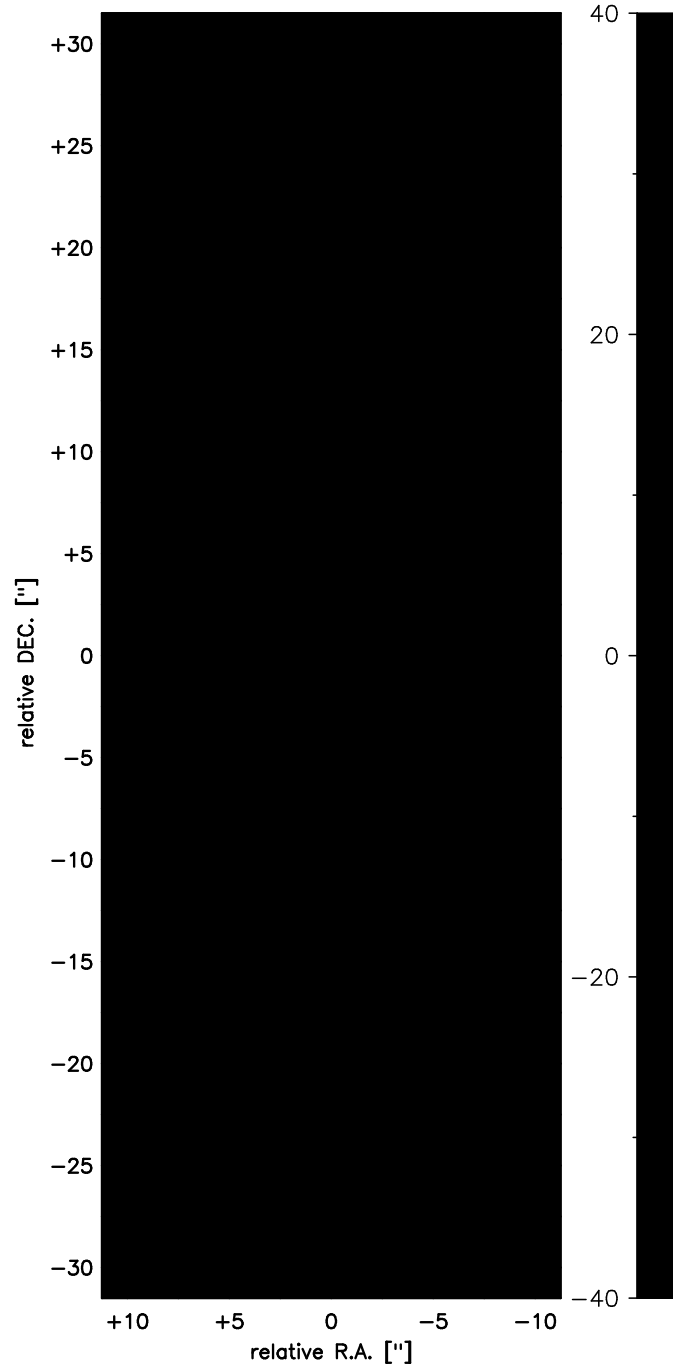


Fig. 9.— Residual velocity field. A model velocity field obtained from the rotation curve was subtracted from the observed velocity field. Large residuals are associated with the gas lanes indicating streaming motion. Only small residuals are seen in the inner 8" demonstrating that the assumption of a rotating disk is a good approximation.

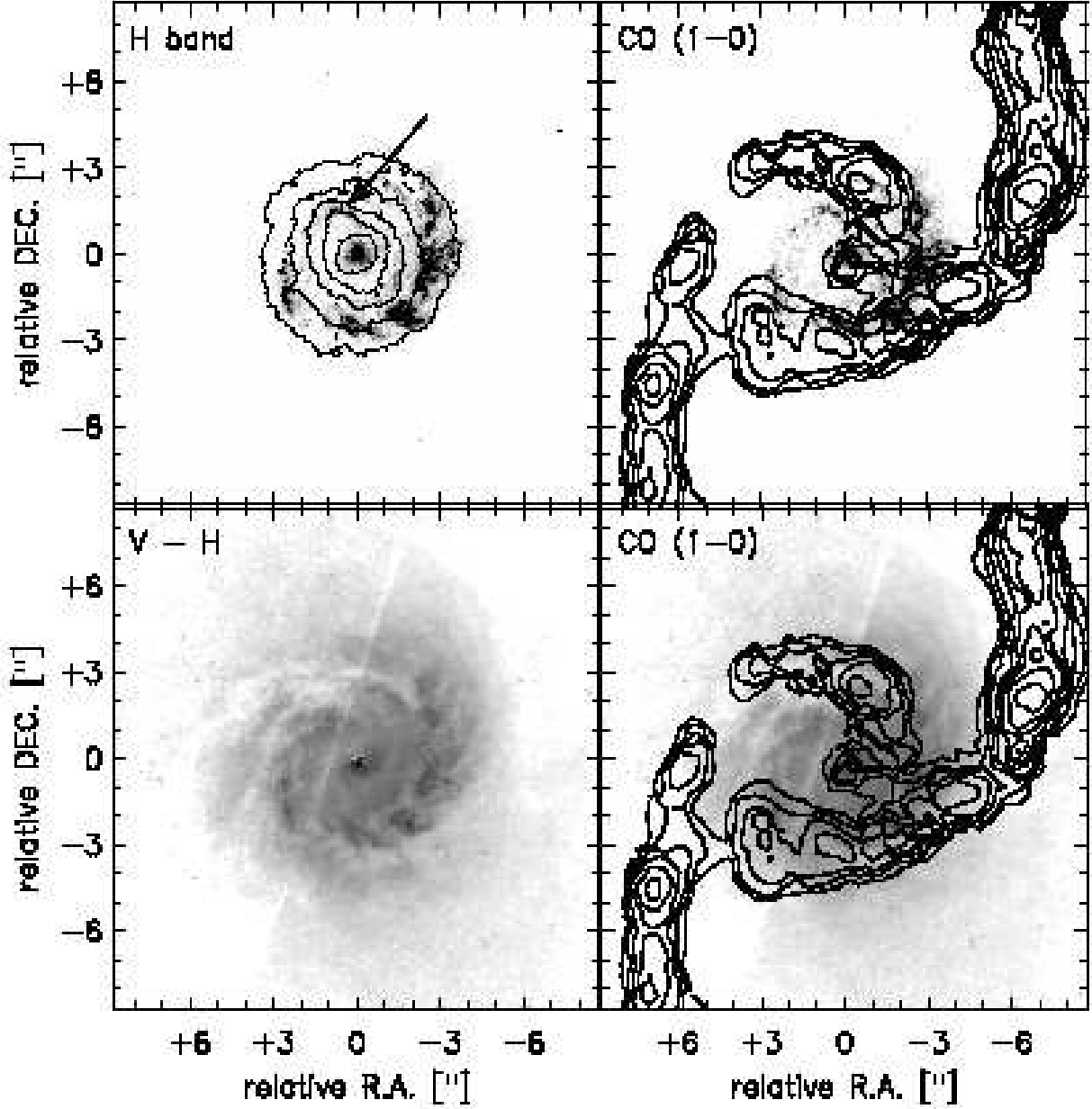


Fig. 10.— Comparison of the stellar clusters seen in the UV continuum (gray-scale, *top*) to the inner bar seen in the HST H band (contours at 5%, 10%, 15%, 20% and 30% of peak value, *top left*), and the ^{12}CO line emission (contours at 20%, 30%, ... , 90% of peak value, *top right*). The extinction can be seen in the HST $V - H$ map (blue colors are darker, *bottom left*) in comparison to the ^{12}CO line emission (contours at 20%, 30%, ... , 90% of peak value, *bottom right*). The arrow in the *top left* panel indicated the string of UV continuum which lies along the NIR bar and is discussed in Section 6.

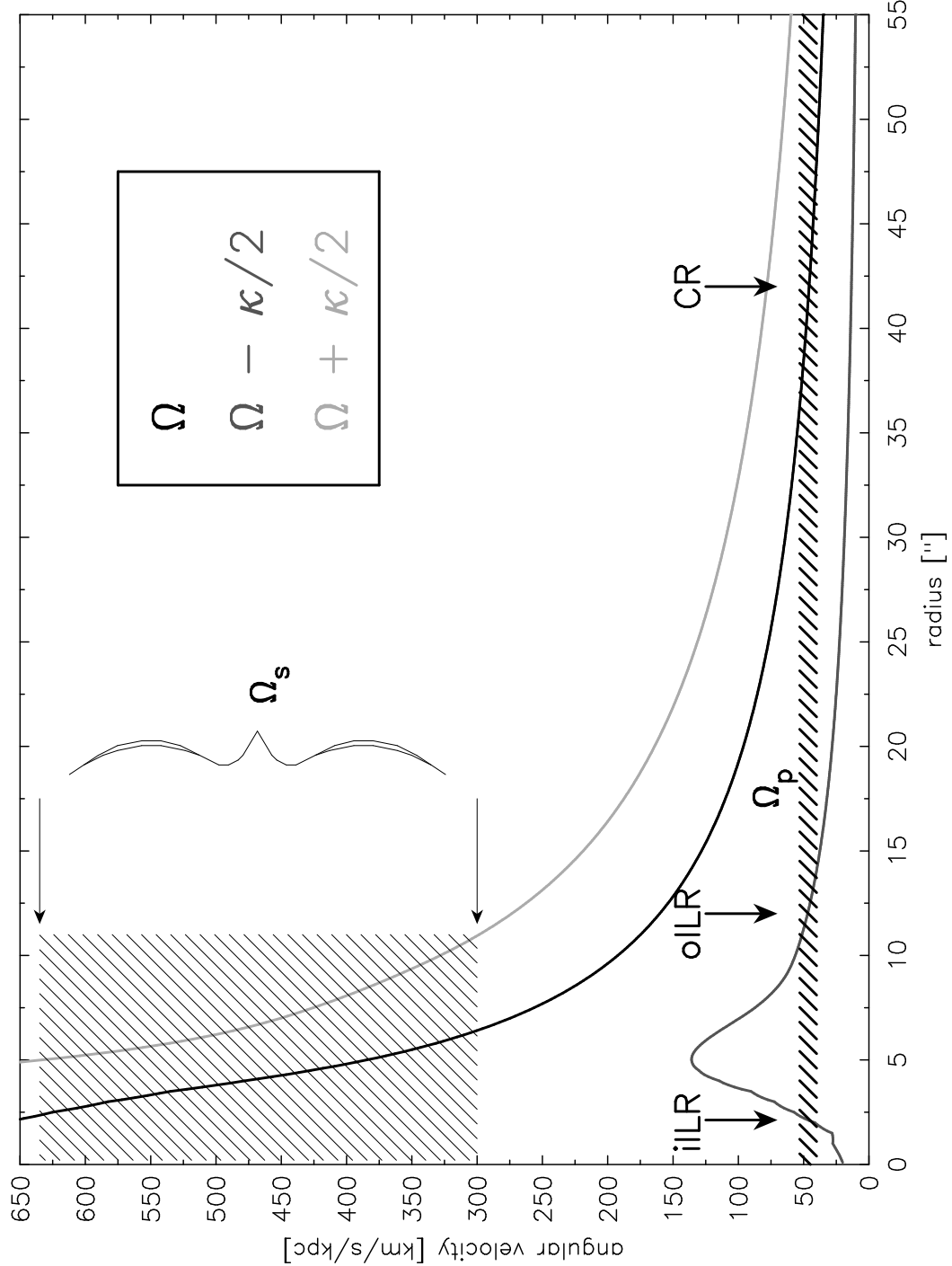


Fig. 11.— Positions of the dynamical resonances in NGC 4303. Assuming a corotation resonance (CR) at about 40'' (see text) implies a (primary) bar pattern speed of $\Omega_p \sim 40 \text{ km s}^{-1} \text{ pc}^{-1}$. Since the rotation velocity is only estimated in the radial range between 4'' and 30'', the position for the outer inner Lindblad resonance (oILR) of the (primary) bar is roughly at about 12''. The position of the inner ILR (iILR), however, is well determined within the errors. The range for possible pattern speed of the smaller (secondary) bar Ω_s is indicated by the hatched area, assuming that the CR of the secondary bar lies within the ILR of the primary bar.

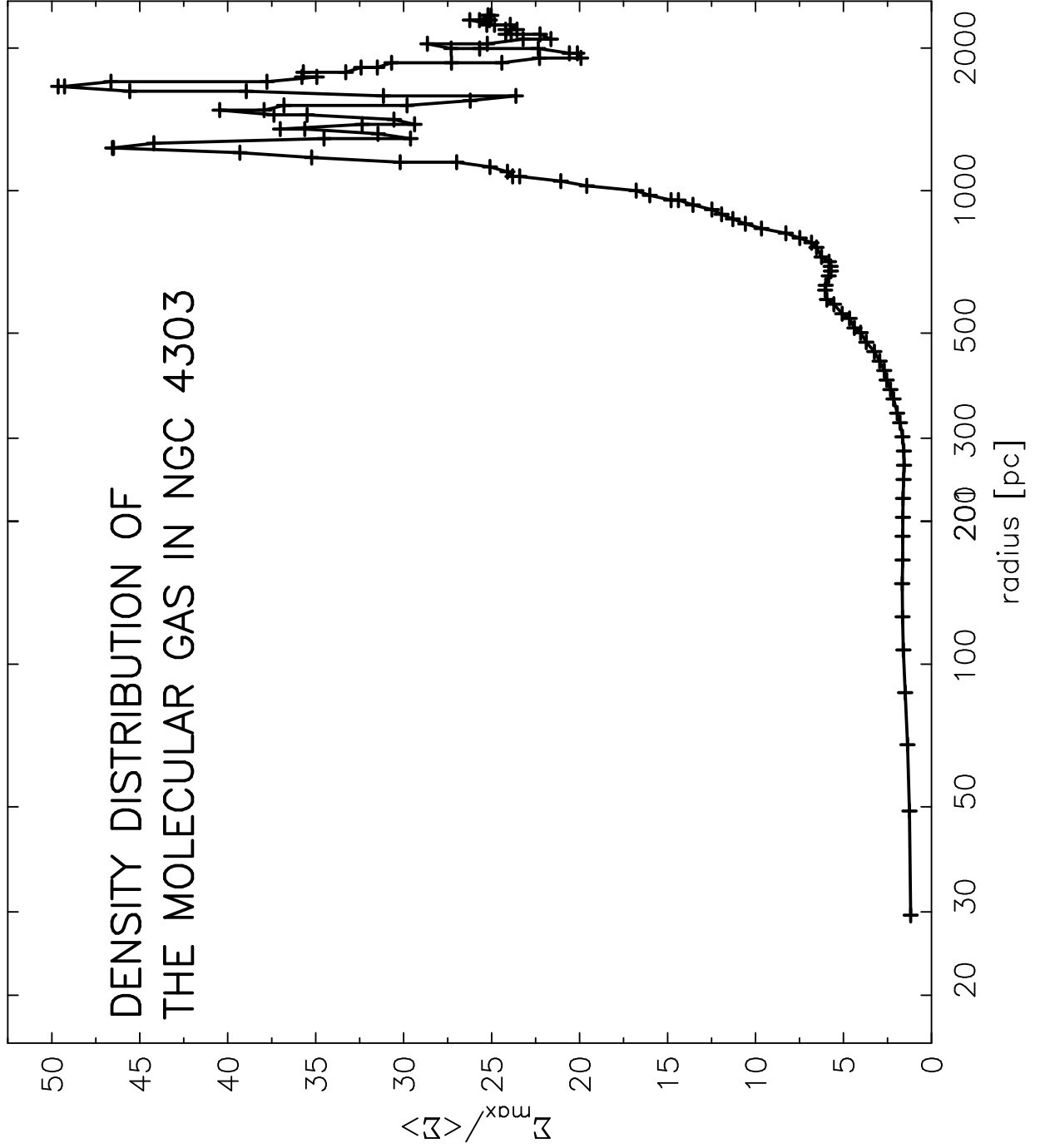


Fig. 12.— The ratio of the maximum emission and the average emission (derived from the 0th moment map of the primary beam corrected data) clearly shows the damping of the shock inside the transition radius $R_t \sim 5''$. This can be compared directly to the density ratio assuming that the ^{12}CO emission is proportional to the molecular hydrogen column density.

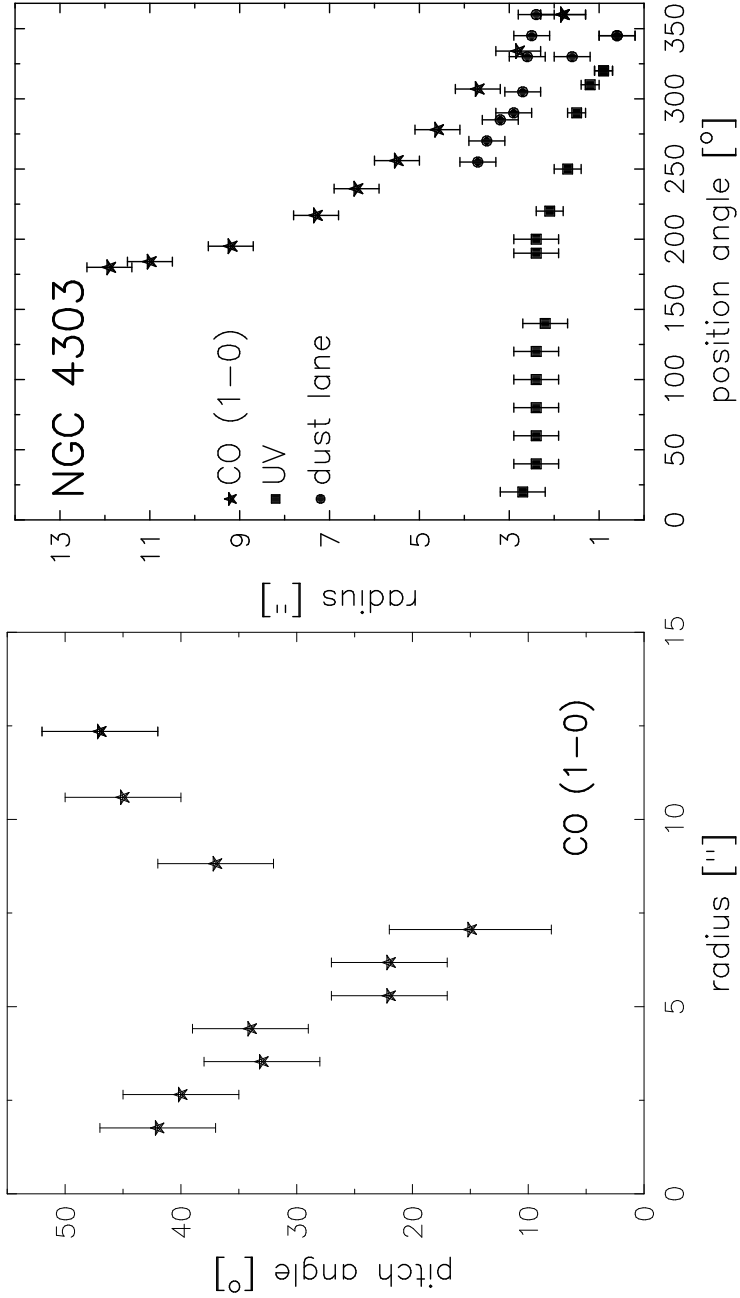


Fig. 13.— *Left*: Pitch angle of the molecular gas spirals (black points) in the inner 15". The angle was measured by eye on the northern spiral arm in the deprojected deconvolved intensity map (see Fig. 14). *Right*: A change of radius with position angle is also indicating a spiral pattern. The radius was measured for different position angle in the deprojected images for the northern CO spiral arm (stars), the UV clusters (squares), and the dust lanes seen in the $V - H$ map (circles). The position angle starts at the (deprojected) major axis and is counted clock-wise. The UV clusters at a PA of 0° form a continuation of the dust lane at PA of 360° . For the position angles of 330° and 345° , we give two measured points for the dust lanes, since the dust lane splits into two parts for these angles. See Section 6 for further discussion.

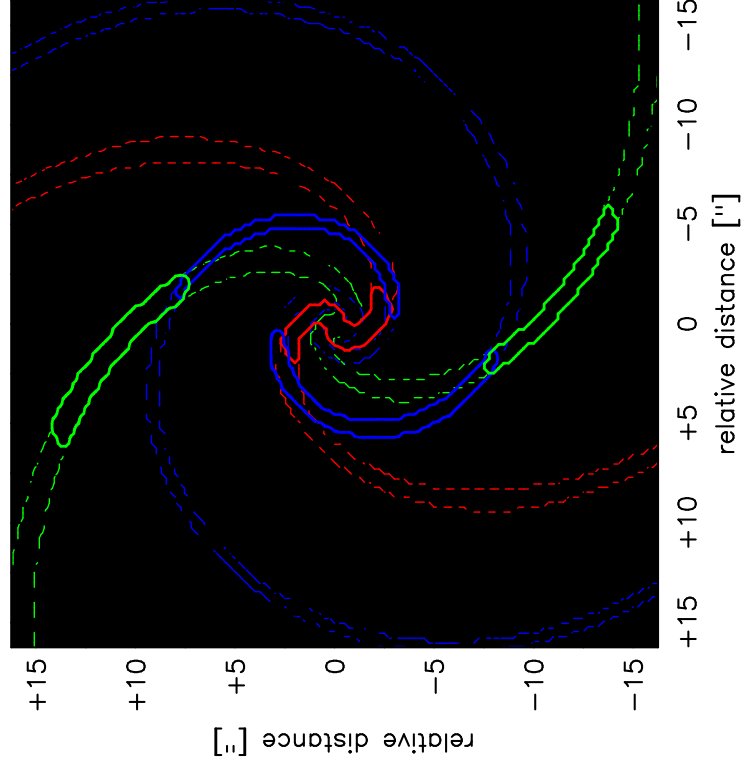


Fig. 14.— Logarithmic spirals with fixed pitch angles of 40° (red contours), 20° (blue contours) and 45° (green contours) are overlaid on the deprojected ^{12}CO 0th moment map (gray-scale). The part of the logarithmic spirals which was fitted to the ^{12}CO data is in solid lines whereas the rest is shown in broken lines. The deconvolved (LUCYed) map which was used to fit the pitch angle is shown in black contours. The required change of the pitch angle for various radii (see Fig. 13) is quite obvious. The major kinematic axis is now running north-south due to the deprojection. This implies that the northern spiral arm is now the eastern one.

Table 1: Summary of the HST Archival data of the nuclear region of NGC 4303.

Dataset	Filter	λ_{cent} [μm]	Exposure [s]
	NUV-MAMA	0.2	3×520
	F606W	0.6	2×160
	F160W	1.6	320

Table 2: Some properties of NGC 4303 (= M 61)

	NGC 4303
Right ascension (J2000)	$12^h 21^m 54.99^s$
Declination (J2000)	$04^\circ 28' 25.55''$
Classification	SAB(rs)bc
Inclination	25°
Position angle	318°
AGN type	LINER/Sey 2
Systemic velocity v_{LSR}	1560 km s^{-1}
Distance	16.1 Mpc
$1''$ equals	78 pc

The sky coordinates, the systemic velocity, and the AGN type were taken from NED (NASA/IPAC Extragalactic Database). The classification is from the RC3 catalog (de Vaucouleurs et al. 1991). Inclination and position angle are described in Section 3.3. For the distance we adopted the value of M 100, the largest spiral in the Virgo cluster (16.1 Mpc, Ferrarrese et al. 1996).

Table 3: ^{12}CO fluxes and Molecular Gas Masses

Component	I_{CO} [Jy km s $^{-1}$]	S_{CO} [K km s $^{-1}$]	N_{H_2} [10^{22}cm^{-2}]	M_{H_2} [$10^7 M_{\odot}$]
Northern peak	18.1	420	8.4	2.4
Southern peak	5.7	131	2.6	0.8
western gas lane (north)	3.4	80	1.6	0.5
western gas lane (south)	53.3	1240	24.7	7.2
eastern gas lane (north)	30.1	700	13.9	4.0
eastern gas lane (south)	2.4	55	1.1	0.3
Northern spiral arm	26.5	615	12.3	3.6
Southern spiral arm	14.3	330	6.6	1.9
Nucleus	6.9	160	3.2	0.9
Nuclear Disk	51.2	1190	23.8	6.9

The ^{12}CO 1 – 0 line fluxes and molecular gas masses for various components of the molecular gas distribution. The components are indicated in Fig. 3. Note, that the molecular gas masses have an uncertainty of a factor of about 2 - 3 due to the uncertainty in the $\frac{N_{H_2}}{I_{CO}}$ conversion factor.